



# A plasmonic Z-scheme Ag@AgCl/PDI photocatalyst for the efficient elimination of organic pollutants, antibiotic resistant bacteria and antibiotic resistance genes

Xue Chen<sup>a,b,c,d</sup>, Zhouping Wang<sup>a,b,c,d,e</sup>, Xuancheng Shen<sup>a,b,c,d</sup>, Yan Zhang<sup>f</sup>, Yang Lou<sup>g</sup>, Chengsi Pan<sup>g</sup>, Yongfa Zhu<sup>h</sup>, Jing Xu<sup>a,b,c,d,\*</sup>

<sup>a</sup> State Key Laboratory of Food Science and Technology, Jiangnan University, Wuxi 214122, PR China

<sup>b</sup> School of Food Science and Technology, Jiangnan University, Wuxi 214122, PR China

<sup>c</sup> International Joint Laboratory on Food Safety, Jiangnan University, Wuxi 214122, PR China

<sup>d</sup> Collaborative Innovation Center of Food Safety and Quality Control in Jiangsu Province, Jiangnan University, Wuxi 214122, PR China

<sup>e</sup> National Engineering Research Center for Functional Food, Jiangnan University, Wuxi 214122, PR China

<sup>f</sup> Jiangsu Key Laboratory of Anaerobic Biotechnology, School of Environment and Civil Engineering, Jiangnan University, Wuxi 214122, PR China

<sup>g</sup> Key Laboratory of Synthetic and Biological Colloids, Ministry of Education, School of Chemical and Material Engineering, Jiangnan University, Wuxi 214122, PR China

<sup>h</sup> Department of Chemistry, Tsinghua University, Beijing 100084, PR China

## ARTICLE INFO

### Keywords:

Supramolecular perylene diimide  
Plasmonic photocatalyst  
Organic pollutants  
Antibiotic resistant bacteria  
Antibiotic resistance genes

## ABSTRACT

Herein, a plasmonic Z-scheme Ag@AgCl/PDI photocatalyst was successfully synthesized by an in-situ deposition-photoreduction method. The loading of Ag@AgCl nanoparticles could improve the light absorption ability of self-assembled perylene diimide (SA-PDI) via the SPR effect. Ag nanoparticles as electron traps could effectively capture photogenerated electrons on the conduction band of SA-PDI, while the Schottky barrier formed by Ag<sup>0</sup> could promote SPR-excited electrons to transfer from Ag to AgCl, further accelerating the charge separation. Besides, more reactive species ( $\bullet\text{O}_2$ ,  $^1\text{O}_2$ ,  $\text{h}^+$  and  $\bullet\text{OH}$ ) could be produced to enhance the oxidation capacity of composite. Therefore, compared with SA-PDI, Ag@AgCl/PDI exhibited more remarkable visible-light photocatalytic performance for the elimination of organic pollutants, antibiotic resistant bacteria (ARB) and antibiotic resistance genes (ARGs). The degradation rates of optimum Ag@AgCl/PDI-3% towards phenol, bisphenol A, sulfadimethoxine and ofloxacin were approximately 5.7, 4.0, 3.2 and 10.0 times higher than those of SA-PDI, respectively. Meanwhile, Ag@AgCl/PDI-3% killed all sulfonamide ARB within 2 h and inactivated 99.6% of sulfonamide ARGs (*sulI*) within 8 h, while SA-PDI only removed 49.4% of ARB and 49.9% of *sulI*. This study could provide a new strategy to design high-efficiency PDI-based photocatalysts for environmental remediation.

## 1. Introduction

In the last few decades, the wastewater containing phenolic organics and antibiotics, as one kind of the most harmful industrial wastewater in the world, has caused serious environmental pollution problems [1]. Phenolic compounds, as highly toxic and hazardous organics, could remain in wastewater for a long time due to its resistant to biodegradation, which can pose a threat to humans and other living organisms even at a low concentration [2–4]. Moreover, as a result of the extensive use of antibiotics, a significant amount of antibiotic-containing effluent from the medical industry and aquaculture is also discharged into the environment, seriously polluting the ecosystem. Since these antibiotics

and their transformation products are hard to degrade naturally, they would exacerbate the issue of antibiotic resistance. Recent studies have shown that antibiotic resistant bacteria (ARB) and antibiotic resistance genes (ARGs) are widespread in medical effluent, aquaculture effluent, drinking water, surface water and groundwater [5–7]. What's worse, ARB and ARGs can interact with humans through the food chain, which will lead to the development of antibiotic resistance and further increase the disease morbidity/mortality [8]. In addition, ethylene, an endogenous plant hormone, is pervasive in all plant tissues. However, excess ethylene can speed up the ripening of fruits and vegetables, causing rapid aging and quality deterioration, which in turn shorten the shelf life and result in huge economic loss [9]. As mentioned above, these

\* Corresponding author at: State Key Laboratory of Food Science and Technology, Jiangnan University, Wuxi 214122, PR China.

E-mail address: [xujing823@jiangnan.edu.cn](mailto:xujing823@jiangnan.edu.cn) (J. Xu).

<https://doi.org/10.1016/j.apcatb.2022.122220>

Received 4 September 2022; Received in revised form 23 November 2022; Accepted 25 November 2022

Available online 26 November 2022

0926-3373/© 2022 Elsevier B.V. All rights reserved.

chemical and biological pollutants need to be addressed urgently due to their enormous threat to ecological environment and human health. Traditional biochemical wastewater processing techniques including physical adsorption, biological treatment and chlorine disinfection methods still have varieties of limitations, such as high cost, low efficiency and secondary pollution. Thus, it is of great importance to develop an advanced oxidation technology with the advantages of highly efficient, cost effective and environmentally friendly for the removal of both chemical and biological pollutants [10]. Solar energy, as a renewable and clean energy source, is currently the best choice for achieving sustainable development of energy and environment. Photocatalysis technology can be regarded as the optimal strategy for solar-to-chemical energy conversion based on semiconductor materials [11,12]. Due to the strong oxidation capacity, low energy consumption, no secondary pollution and mild reaction conditions, semiconductor photocatalysts have been extensively investigated in recent years and shown a good promise in the elimination of organic pollutants [13,14], ARB [15] and ARGs [16].

Compared to inorganic materials, organic semiconductor materials have many irreplaceable advantages, such as greater structural tunability, broader spectral response range and more source of raw materials [17]. Perylene diimide (PDI), which has excellent stability, high electron affinity and fast charge mobility, stands out among n-type organic semiconductors [18–20]. In 2016, Liu et al. reported a self-assembled PDI with non-substituents (PDINH) supramolecular system consisting of purely organic PDINH molecular units through non-covalent interactions, exhibited a band-like electronic energy level structure and a long-range conjugated  $\pi$ -delocalization, which displayed excellent performance in phenol degradation and  $O_2$  evolution under visible light irradiation [21]. However, the photocatalytic activity of supramolecular PDI prepared by the self-assembly method is not satisfactory due to the high recombination rate of electron-hole ( $e^-h^+$ ) pairs. To solve this problem, researchers have compounded self-assembled PDI (SA-PDI) with other semiconductors to form suitable heterojunction photocatalysts with more outstanding performance. Yang et al. constructed an efficient full-spectrum responsive p-Ag<sub>2</sub>S/n-PDI heterojunction photocatalyst by tightly loading Ag<sub>2</sub>S quantum dots onto the surface of SA-PDI nanofibers through a two-step electrostatic process, which facilitated the migration of photogenerated electrons along the quasi-one-dimensional  $\pi$ - $\pi$  stacking of SA-PDI and further broadened the spectral response range of SA-PDI. Compared with SA-PDI, p-Ag<sub>2</sub>S/n-PDI heterojunction exhibited a much stronger oxidation ability owing to its more production of active species [22]. Another effective strategy to inhibit the charge recombination and improve the light absorption ability of SA-PDI is decorating with noble metal nanoparticles, such as Au and Ag [23]. Miao et al. prepared Au/PDI photocatalyst by electrostatic adsorption. Compared with SA-PDI, the Au/PDI composite exhibited superior photocatalytic degradation towards phenol, indicating that the SPR effect of Au nanoparticles could not only effectively increase the charge migration rate, but also significantly improve the photocatalytic efficiency and solar energy utilization of SA-PDI [24].

In recent years, the construction of the Z-scheme heterojunction is also considered to be an efficient pathway to improve the catalytic activity of photocatalyst. In a Z-scheme heterojunction system, two semiconductors with interlaced energy band structures can be assembled by an oxidative semiconductor with higher valence band potential and a reductive semiconductor with lower conduction band potential. Under light irradiation, the electrons in conduction band of oxidative semiconductor recombine with the holes in valence band of reductive semiconductor, thus preserving the minimum conduction band and the maximum valence band in each two components. Thus, Z-scheme heterojunctions exhibit more reinforced spatial charge separation and boosted redox ability than conventional heterojunctions [25,26]. Ag/AgCl, as a typical plasmonic composite photocatalyst, shows excellent visible-light photocatalytic activity and stability [27]. Moreover, according to previous studies, Ag/AgCl has been reported as an effective

component to modify other semiconductors to construct Z-scheme photocatalysts [28,29]. The SPR effect of Ag nanoparticles (AgNPs) can introduce a new source of light absorption, while the matched band structure between Ag/AgCl and another semiconductor can improve the spatial carriers separation and strengthen the redox ability, thus greatly enhancing the visible-light photocatalytic performance of the composites [30]. Besides, as a noble metal, AgNPs could act as a bridge to improve the interfacial charge migration efficiency and mediate the interfacial electron transfer direction, thus enhancing the stability of charge transfer process in Z-scheme heterojunctions [31]. Therefore, the Ag-bridged Z-scheme heterojunctions containing three components were found to possess highly stable charge transfer process and remarkably enhanced photocatalytic performance. For instance, Liu et al. synthesized Ag/AgCl@MIL-53-Fe by immobilizing Ag/AgCl nanoparticles on the surface of MIL-53-Fe microrods. The Z-scheme heterojunction structure of this composite photocatalyst prolonged the lifetime of photogenerated carriers, thus achieving highly efficient organic pollutant degradation and Cr(VI) reduction of Ag/AgCl@MIL-53-Fe [32]. In addition, AgNPs have shown broad-spectrum and potent antibacterial activity through destroying functional biomolecules and cellular metabolic processes [33]. Furthermore, researches have demonstrated that Ag/AgCl nanoparticles can be dispersed on other semiconductors to achieve extremely effective disinfection performance via a synergistic antibacterial mechanism [34, 35]. Inspired by the abovementioned reasons, we hypothesize the introduction of Ag@AgCl to the SA-PDI supramolecular system to further improve the photocatalytic performance for the removal of organic pollutants, ARB and ARGs.

In this work, Ag@AgCl/PDI composite with strong light absorption ability, rapid carrier separation efficiency and high oxidation capacity was successfully prepared by an in-situ deposition-photoreduction method. The morphology, crystalline structure, chemical state and optoelectronic properties of Ag@AgCl/PDI were carefully investigated. The photocatalytic oxidation performance of Ag@AgCl/PDI was evaluated by the removal of phenolic compounds, antibiotics, ethylene, sulfonamide ARB and ARGs. In addition, the mechanism of the boosted photocatalytic performance of Ag@AgCl/PDI system was further elucidated by investigating the roles of Z-scheme heterostructure and SPR effect on the behavior of photogenerated carriers.

## 2. Experimental section

### 2.1. Preparation of Ag@AgCl/PDI

Ag@AgCl/PDI composite was prepared via an in-situ deposition-photoreduction method. SA-PDI was synthesized by a supramolecular self-assembly approach described in the [Supplementary Material](#). 100 mg SA-PDI was dispersed in methanol by ultrasound for 30 min. A certain volume of AgNO<sub>3</sub> methanol solution (1.574 mg/mL) was added and stirred for 0.5 h in the dark. Then a certain volume of NaCl methanol solution (0.133 mg/mL) (the volume ratio of AgNO<sub>3</sub> to NaCl solution is 1.0:2.5) was added to the mixture and stirred in the dark for another 0.5 h. Afterwards, the above dispersion was stirred for 3 h under the irradiation of a 10 W LED lamp (100 mW/cm<sup>2</sup>,  $\lambda > 400$  nm). The obtained precipitate was collected by centrifugation, washed with methanol, and dried under vacuum at 60 °C for 24 h. The final product was labeled as Ag@AgCl/PDI-X, X represented the mass percentage of Ag to SA-PDI, X = 1%, 2%, 3%, 4% and 5%.

### 2.2. Photocatalytic degradation experiments

Phenol, bisphenol A (BPA), sulfadimethoxine (SDM) and ofloxacin (OFX) were used as the model pollutants to evaluate the photocatalytic degradation activity of Ag@AgCl/PDI in the liquid phase system. The photocatalytic reaction was carried out in a multi-channel photoreaction apparatus (Pefectlight PCX50C). Visible light was provided by a Vlight

multi-channel lamp panel equipped with 10 W LED lamps (100 mW/cm<sup>2</sup>,  $\lambda > 400$  nm). 10 mg photocatalyst powder was dispersed in 50 mL 5 ppm phenol solution/10 ppm BPA solution/10 ppm SDM solution/20 ppm OFX solution by sonication for 30 min and stirred for 30 min in the dark to reach the adsorption-desorption equilibrium. Under visible light irradiation, 2 mL of the reaction mixture was sampled at regular intervals, and the photocatalyst was removed by centrifugation and filtration with a 0.22  $\mu$ m membrane filter. The concentrations of phenol, BPA, SDM and OFX were determined by high performance liquid chromatography (HPLC) equipped with a Waters-C18 column (1 mL/min). The detailed HPLC analysis parameters were listed in Table S1. Moreover, the ethylene degradation was carried out to evaluate the photocatalytic activity of Ag@AgCl/PDI in the gas phase system. 20 mg sample powder was ultrasonically dispersed in 4 mL ultrapure water. The suspension was coated on both sides of the glass slide (70  $\times$  20  $\times$  1 mm), dried at room temperature and heated at 180  $^{\circ}$ C for 5 h. The glass slide was placed in a quartz bottle, sealed and injected 10 mL 0.05% ethylene gas. The ethylene concentration was analyzed using gas chromatography (GC) (Shimadzu GC-2014, Japan) with Rtx-1 chromatographic column and a flame ionization detector (FID).

### 2.3. Photocatalytic inactivation of ARB

Sulfonamide ARB were selected as the model ARB for the photocatalytic antibacterial experiments. Environmental water sample was collected from Jiangnan University campus and stored at 4  $^{\circ}$ C before use. The water sample was cultured on Luria Bertani (LB) solid medium containing 512 mg/L SDM. The inoculated plates were incubated at 37  $^{\circ}$ C for 24 h. Individual colonies were randomly selected and scribed on LB solid medium. The isolates were purified several times to obtain sulfonamide ARB. The obtained sulfonamide ARB isolates were cultured in LB nutrient solution at 37  $^{\circ}$ C for 4 h. Then the culture medium was removed by centrifugation at 4000 rpm for 5 min at 4  $^{\circ}$ C, washed twice with sterile 0.9% saline, and then resuspended in sterilized saline. The sulfonamide ARB density was  $1 \times 10^7$  cfu/mL, and the concentration of photocatalyst was 0.2 g/L. The photocatalytic inactivation reaction was carried out in a multi-channel photoreaction apparatus (Pefectlight PCX50C). Visible light was provided by a Vlight multi-channel lamp panel equipped with 10 W LED lamps (100 mW/cm<sup>2</sup>,  $\lambda > 400$  nm). Under visible light irradiation, aliquots of bacterial solution were pipetted every 0.5 h and diluted with sterilized saline. 100  $\mu$ L of diluent suspension was spread on LB agar plates and cultured at 37  $^{\circ}$ C for 12 h. The viable sulfonamide ARB densities (in CFU) were estimated by colony counting method. Light group (without photocatalyst) and dark group (Ag@AgCl/PDI-3% without light) were set up. Each group was carried out in triplicate. The experimental apparatus and saline solution were sterilized at 121  $^{\circ}$ C for 20 min.

### 2.4. Photocatalytic inactivation of ARGs

In this study, sulfonamide ARGs (*sul1*) were selected as the model for the photocatalytic inactivation of ARGs under the irradiation of a 300 W xenon lamp (CEL-HXF300) with a 400 nm cut-off filter (150 mW/cm<sup>2</sup>). 50 mg photocatalyst was added to 200 mL environmental water sample and stirred for 8 h under visible light irradiation. After the reaction, the suspension was filtered through a 0.45  $\mu$ m filter membrane filter to collect the DNA. Then the obtained DNA was extracted using a soil DNA extraction kit (TIAGEN) and stored at -20  $^{\circ}$ C. The ratio of OD260/OD280 and the concentration of DNA were measured by a Nanodrop spectrophotometer with Nanodrop-2000c software. Real-time quantitative PCR (qPCR) analysis was used to quantify the absolute abundance of ARGs. The primers and reaction conditions used for qPCR procedure have been reported in previous study [36,37], which were shown in Table S2. The qPCR amplification reaction was performed on a StepOnePlus (ABI) instrument in a 20  $\mu$ L reaction system containing 10  $\mu$ L SYBR Green I (SYBR Green qPCR Mastermixes, QIAGEN), 1  $\mu$ L each

primer, 1  $\mu$ L DNA template and replenish to 20  $\mu$ L with sterilized double distilled water. A standard curve for estimating the absolute abundance of ARGs in the samples was constructed based on the known copy number standard plasmids at 10-fold gradient dilutions. The qPCR reaction procedures were as follows: initial denaturation at 95  $^{\circ}$ C for 7 min, followed by 40 cycles of denaturation at 95  $^{\circ}$ C for 10 s and primer annealing at 60  $^{\circ}$ C for 34 s. Finally, the melting curve was examined with temperature ramping from 60  $^{\circ}$ C to 95  $^{\circ}$ C. Each group was run in triplicate.

## 3. Results and Discussion

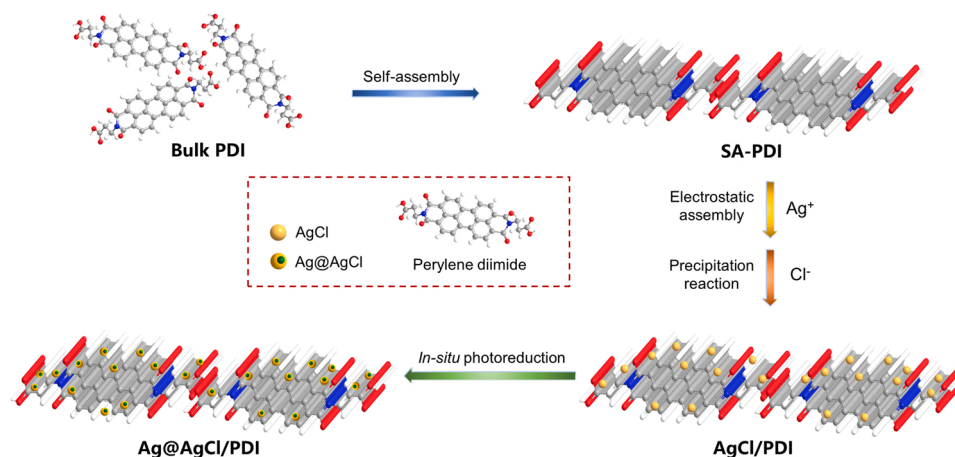
### 3.1. Characterization of Ag@AgCl/PDI composite photocatalysts

The preparation strategy of Ag@AgCl/PDI composite photocatalysts was illustrated in Scheme 1. Firstly, bulk PDI was dissolved in alkaline TEA solution and subsequently self-assembled into SA-PDI with supramolecular structure through  $\pi$ - $\pi$  interaction between PDI molecules and hydrogen bonding between carboxylic acid groups after the addition of HCl solution [38]. Subsequently, AgCl nanoparticles were deposited on the surface of SA-PDI through electrostatic assembly and precipitation reaction between Ag<sup>+</sup> from AgNO<sub>3</sub> and Cl<sup>-</sup> from NaCl. Finally, part of Ag<sup>+</sup> in AgCl was reduced to Ag<sup>0</sup> via an in-situ photoreduction reaction to form Ag@AgCl/PDI composite photocatalysts. The morphologies of the samples were observed by transmission electron microscope (TEM) and high-resolution TEM (HRTEM). As shown in the TEM images (Fig. 1a-b), SA-PDI exhibits well-defined nanofiber structure with a diameter of ~20–40 nm and a length of ~100–400 nm, while Ag@AgCl nanoparticles with a size of 10–40 nm were uniformly dispersed on SA-PDI nanofibers. As shown in Fig. 1c, the HRTEM image of Ag@AgCl/PDI presents evident lattice fringes of 0.199 nm and 0.239 nm, which are corresponding to the (220) crystal plane of AgCl and the (111) crystal plane of Ag, respectively, further proving the successful loading of Ag@AgCl nanoparticles [39,40]. As shown in Fig. S1 in the Supplementary Material, the zeta potentials of SA-PDI and Ag@AgCl are -23.1 mV and -18.1 mV, respectively, and the combination makes the zeta potential of Ag@AgCl/PDI-3% change into -21.7 mV.

The crystal phase and molecular structure of the as-synthesized samples were investigated by X-ray diffraction (XRD), Fourier transform infrared spectroscopy (FTIR) and Raman analysis. As shown in Fig. 2a, Ag@AgCl displays the characteristic diffraction peaks at 27.9 $^{\circ}$ , 32.4 $^{\circ}$ , 46.4 $^{\circ}$ , 55.1 $^{\circ}$ , 57.6 $^{\circ}$ , 67.5 $^{\circ}$ , 74.5 $^{\circ}$  and 76.9 $^{\circ}$ , which are attributed to AgCl, while the weak peaks at 38.3 $^{\circ}$  and 44.4 $^{\circ}$  are attributed to Ag [39,41,42]. As the mass ratio of Ag@AgCl increases, the diffraction peaks of Ag@AgCl/PDI composites at 27.9 $^{\circ}$ , 32.4 $^{\circ}$ , 44.4 $^{\circ}$ , 46.4 $^{\circ}$ , 55.1 $^{\circ}$ , 57.6 $^{\circ}$  and 76.9 $^{\circ}$  gradually enhance, indicating that the successful loading of Ag@AgCl in proportion. As observed in the FTIR spectra (Fig. S2a), the peaks of SA-PDI at 1650 cm<sup>-1</sup> and 1690 cm<sup>-1</sup> are attributed to the stretching vibrations of C=C and C=O, respectively, indicating the presence of carboxyl substituents and benzene ring structure in the framework of SA-PDI, while Ag@AgCl shows no obvious absorption peaks. As observed in the Raman spectra (Fig. S2b), the peaks of SA-PDI located at 1590 cm<sup>-1</sup> and 1302 cm<sup>-1</sup> can be respectively corresponding to the C=C/C-C and C-H stretching vibrations in the benzene ring. The FTIR and Raman spectra of Ag@AgCl/PDI composites are almost similar to those of SA-PDI, demonstrating that the loading of Ag@AgCl has no influence on the molecular structure of SA-PDI.

The light absorption ability of Ag@AgCl/PDI composites were characterized by UV-Vis diffuse reflectance spectra (DRS). As shown in Fig. 2b, Ag@AgCl has a broad absorption peak in the range of 400–800 nm due to the SPR effect of AgNPs, and the spectral response range of SA-PDI covers almost the whole visible region. In contrast, the modification of Ag@AgCl significantly improves the visible light absorption ability of Ag@AgCl/PDI composites in the region of 420–620 nm due to the presence of SPR effect, thus effectively enhancing the solar light utilization efficiency [43–45]. The MS plots of





Scheme 1. Schematic illustration of synthesizing Ag@AgCl/PDI composite photocatalysts.

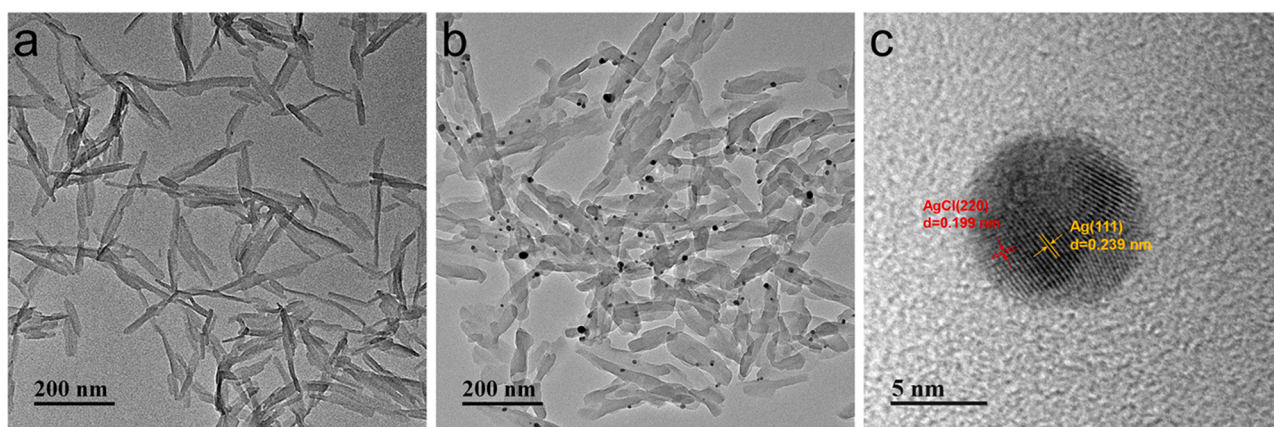


Fig. 1. TEM images of (a) SA-PDI and (b) Ag@AgCl/PDI-3%. (c) HRTEM image of Ag@AgCl/PDI-3%.

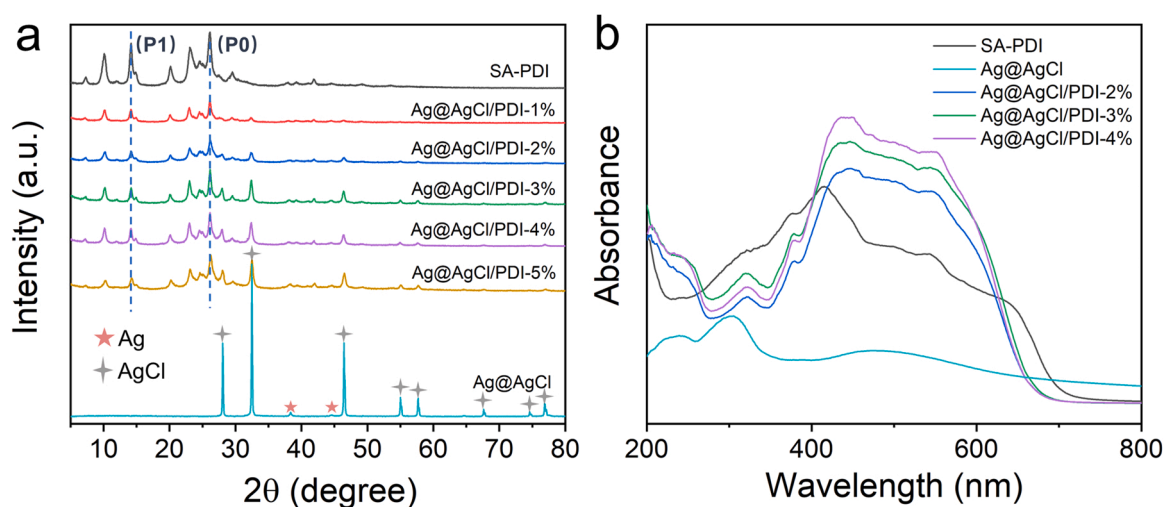


Fig. 2. (a) XRD patterns of Ag@AgCl, SA-PDI and Ag@AgCl/PDI. (b) DRS of Ag@AgCl, SA-PDI and Ag@AgCl/PDI.

SA-PDI (Fig. S3) shows an S-shape with positive slope, indicating that SA-PDI is an n-type semiconductor [46]. The flat-band potential ( $E_{fb}$ ) of SA-PDI is estimated to be  $-0.24$  V (vs. SCE) based on the intersection of the  $Cs^{-2}$ -0 linear potential curve. The conduction band edge potential ( $E_{CB}$ ) is calculated according to the following equation:  $E_{CB}$  (NHE, pH = 7) =  $E_{fb}$  (SCE, pH = 7) +  $0.24 - 0.20$ , thus the  $E_{CB}$  of SA-PDI is  $-0.20$  V

(vs. NHE) [47]. As the band gap energy ( $E_g$ ) value of SA-PDI was reported to be  $1.69$  eV, the valence band edge potential ( $E_{VB}$ ) of SA-PDI is calculated to be  $1.49$  V (vs. NHE) based on the equation of  $E_{VB} = E_{CB} + E_g$  [38]. According to previous research work, the CB and VB energy levels of AgCl are located at  $-0.13$  V (vs. NHE) and  $3.02$  V (vs. NHE), respectively [48]. Since the CB and VB positions of AgCl are both higher



than that of SA-PDI, it is feasible to fabricate an efficient and stable Z-scheme heterojunction between Ag@AgCl and SA-PDI. In addition, the matching energy band structures of Ag@AgCl/PDI can lead to a built-in electric field at the interfaces, which are favorable to the charge separation.

The surface chemical compositions and valence bonds of the samples were investigated by X-ray photoelectron spectroscopy (XPS) analysis [49]. As shown in the survey spectra (Fig. 3a), SA-PDI consists of C, N and O elements, while Ag@AgCl/PDI-3% is comprised of C, N, O, Ag and Cl elements. The C 1s spectrum of SA-PDI (Fig. 3b) shows the presence of four peaks at 284.8 eV, 286.3 eV, 287.8 eV and 289.2 eV, corresponding to the C in C-C, C-N, C=O and  $\pi$ -excitation bonds, respectively. Compared with SA-PDI, the C=O peak of Ag@AgCl/PDI-3% shifts towards higher binding energy (287.9 eV), suggesting the existence of electron transfer between the SA-PDI and Ag@AgCl. The N 1s spectra of SA-PDI and Ag@AgCl/PDI-3% both reveal an N-C<sub>x</sub> peak at 400.1 eV (Fig. S4a) [47]. The O 1s spectrum of Ag@AgCl/PDI-3% (Fig. S4b) shows three peaks at 533.0 eV, 531.5 eV and 530.8 eV corresponding to the O in adsorbed H<sub>2</sub>O, C-O and C=O bonds, respectively, which are in accordance with those of SA-PDI [50]. As shown in the Ag 3d spectrum (Fig. 3c), Ag@AgCl/PDI-3% exhibits two well-defined peaks at 367.3 eV and 373.3 eV corresponding to Ag<sup>+</sup> 3d<sub>5/2</sub> and Ag<sup>+</sup> 3d<sub>3/2</sub> in AgCl, respectively, and another two peaks at 367.9 eV and 373.9 eV corresponding to Ag<sup>0</sup> 3d<sub>5/2</sub> and Ag<sup>0</sup> 3d<sub>3/2</sub> in the metallic Ag, respectively [29, 39,51]. Based on the XPS analysis, the proportion of metallic Ag in Ag@AgCl is 24.9%, corroborating partial AgCl can be successfully reduced to Ag under visible light irradiation. The Cl 2p spectrum of

Ag@AgCl/PDI-3% (Fig. 3d) shows two peaks at 197.7 eV and 199.2 eV, which are ascribed to Cl 2p<sub>3/2</sub> and Cl 2p<sub>1/2</sub>, respectively [52]. The XPS results further evidence the successful integration of Ag@AgCl and SA-PDI. Moreover, the peaks of Ag<sup>+</sup> 3d (367.5 eV and 373.5 eV) and Cl 2p (197.9 eV and 199.5 eV) of Ag@AgCl shift towards lower binding energy of those of Ag@AgCl/PDI-3%, respectively. The opposite peak shift of (Ag<sup>+</sup> 3d and Cl 2p) and (C 1s) in Ag@AgCl/PDI suggests that the interface charge redistribution upon the formation of heterojunction and the free electron migration from SA-PDI to AgCl via Ag, further confirming the strong interface interaction between Ag@AgCl and SA-PDI [53,54].

### 3.2. Highly efficient photocatalytic oxidation performance of Ag@AgCl/PDI composites

#### 3.2.1. Photocatalytic degradation towards organic pollutants

Phenol was chosen as the main organic pollutant to study the photocatalytic degradation activity of Ag@AgCl/PDI composites. As shown in Fig. S5a, SA-PDI, Ag@AgCl, bulk PDI and g-C<sub>3</sub>N<sub>4</sub> exhibit poor photocatalytic activity, which can only degrade about 33.5%, 26.2%, 8.6% and 11.8% of phenol within 3 h, respectively. In comparison, all the Ag@AgCl/PDI composites display higher degradation activity, which gradually increases and then decreases with the rising amount of Ag@AgCl. Among them, Ag@AgCl/PDI-3% shows the highest degradation activity, which can remove 92.6% of phenol. According to the apparent rate constant (*k*) obtained via fitting the pseudo-first-order kinetic equation (Fig. S5b), Ag@AgCl/PDI-3% possesses the maximum

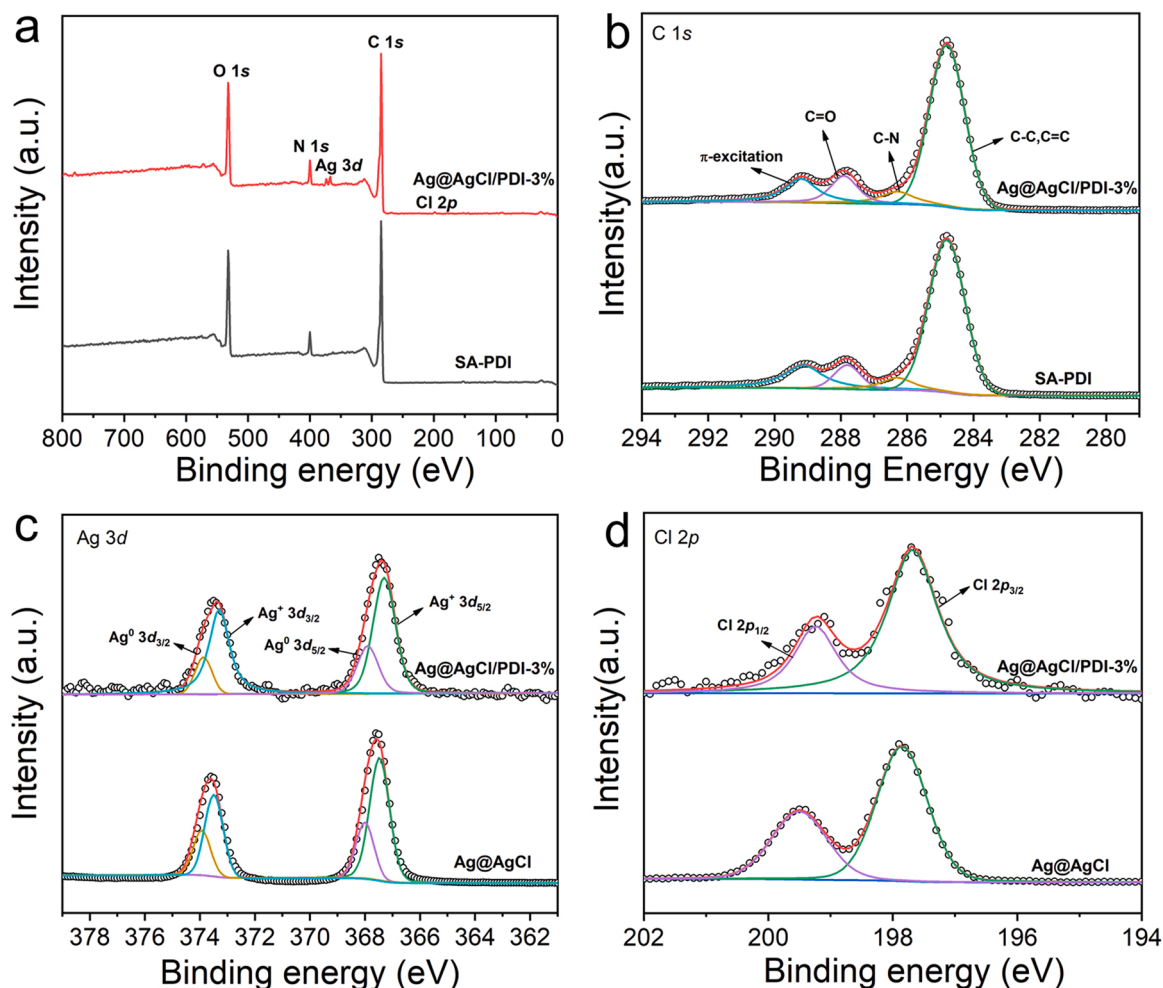


Fig. 3. XPS spectra of SA-PDI and Ag@AgCl/PDI-3%: (a) XPS survey and (b) C 1s. XPS spectra of Ag@AgCl/PDI-3% and Ag@AgCl: (c) Ag 3d and (d) Cl 2p.

$k$  values ( $0.74 \text{ h}^{-1}$ ), which is approximately 5.7, 7.4, 14.8 and 24.7 times as that of SA-PDI ( $0.13 \text{ h}^{-1}$ ), Ag@AgCl ( $0.10 \text{ h}^{-1}$ ), g-C<sub>3</sub>N<sub>4</sub> ( $0.05 \text{ h}^{-1}$ ) and bulk PDI ( $0.03 \text{ h}^{-1}$ ), respectively (Fig. 4a). When the loading ratio exceeds 3 wt%, redundant Ag@AgCl nanoparticles could occupy the active sites on the surface of SA-PDI and thus affect the photocatalytic activity of the composites [55]. The above results indicate that the enhanced photocatalytic performance of Ag@AgCl-PDI is attributed to the synergistic effect between SA-PDI and Ag@AgCl. The intermediates and mineralization ability of Ag@AgCl-PDI for phenol degradation were investigated by HPLC analysis. As revealed in Fig. S6a and S6b, the phenol peak centered at 5 min gradually weakens with the increasing reaction time. Compared with SA-PDI, Ag@AgCl/PDI-3% shows a phenol peak with lower intensity and a larger number of intermediate products after 2 h of degradation, indicating that mineralization ability of Ag@AgCl/PDI has been greatly enhanced. Under the attack of reactive species generated during the photocatalytic process in the composite system, the benzene ring of the phenol molecule can be converted into a variety of aromatic intermediates, such as hydroquinone, catechol, resorcinol and benzoquinone, which would be further decomposed into carboxylic acids through ring-opening reactions and finally mineralized to CO<sub>2</sub> and H<sub>2</sub>O [56]. Furthermore, the photocatalytic activity of Ag@AgCl/PDI-3% towards phenol degradation was investigated under different incident wavelengths of monochromatic light, including 365 nm, 420 nm, 450 nm, 485 nm, 520 nm, 595 nm and 630 nm. As shown in Fig. 4b, the variation tendency of the wavelength-dependent  $k$  values of Ag@AgCl/PDI-3% is in strong agreement with DRS curve, suggesting the light absorption plays a major role in the photocatalytic performance. Since the recyclability of photocatalysts affects the practical application prospect to some extent, we further evaluated the stability of Ag@AgCl/PDI-3% through recycle tests towards phenol degradation under visible light. As shown in Fig. 4c, the degradation efficiency for phenol after four cycles has reduced by about 16.3%. Compared to the first cycle, there is a small decrease in photodegradation activity of Ag@AgCl/PDI-3% in the second cycle due to the adsorption of phenol molecules occupied the active sites of photocatalyst, and the degradation efficiency remains constant in the later cycles, indicating Ag@AgCl/PDI photocatalyst has excellent recyclability. We further evaluated the photocatalytic H<sub>2</sub>O<sub>2</sub> production ability of Ag@AgCl/PDI under visible light in the phenol degradation system. Fig. S7a shows that the standard curve of H<sub>2</sub>O<sub>2</sub> concentration-absorbance measured by the iodometric method is  $y = 0.01134x + 0.01567$  with a  $R^2$  value of 0.9997. As shown in Fig. S7b, the H<sub>2</sub>O<sub>2</sub> yield of Ag@AgCl/PDI-3% is 26.5  $\mu\text{M}$  after 2 h of irradiation, which is about 1.2 times as that of SA-PDI (21.9  $\mu\text{M}$ ), indicating the better H<sub>2</sub>O<sub>2</sub> production ability of the Ag@AgCl/PDI system.

In order to verify the wide applicability of the excellent photodegradation activity of Ag@AgCl/PDI, the degradation experiments towards bisphenol A (BPA), sulfadimethoxine (SDM), ofloxacin (OFX),

and ethylene were also conducted. As shown in Figs. S8 and 5a, Ag@AgCl/PDI-3% possesses the highest determined  $k$  values for BPA, SDM, OFX and ethylene degradation, which are almost 4.0, 3.2, 10.0 and 2.4 times as those of SA-PDI, respectively, and nearly 20.9, 30.5, 65.6, 2.6 times as those of Ag@AgCl, respectively. The above results indicate that Ag@AgCl/PDI shows more excellent degradation performance and good universality for different organic pollutants compared with SA-PDI and Ag@AgCl, which are the required features for the treatment of organic pollution in water environment. As shown in Fig. S9, the degradation efficiencies of Ag@AgCl/PDI-3% for BPA, SDM, OFX and ethylene after four cycles have reduced by about 17.5%, 13.3%, 5.3% and 4.2%, respectively, further proving its good stability. Besides, the XRD pattern, FTIR spectrum and TEM image of Ag@AgCl/PDI-3% after recycle tests are basically similar to those before the photocatalytic reaction (Fig. S10), indicating that the structure of Ag@AgCl/PDI composite is quite stable during the photocatalytic process.

Furthermore, the effect of Ag@AgCl modification on the rate of photon absorption was further evaluated by measuring the photon absorption intensity, the specific extinction coefficient and the optical thickness in the reactor of SA-PDI and Ag@AgCl/PDI suspensions according to the methods reported by previous literatures [57–60]. As shown in Fig. S11a, the photon absorption intensities for SA-PDI and Ag@AgCl/PDI-3% suspensions in a 50 mL phenol solution were measured to be 80.58 mW/cm<sup>2</sup> and 83.71 mW/cm<sup>2</sup>, respectively. As shown in Fig. S11b, since the spectral response range of SA-PDI covers the range of 400–800 nm, the specific extinction coefficients of SA-PDI and Ag@AgCl/PDI-3% were determined as a function of wavelength in the region of 400–800 nm, and Ag@AgCl/PDI-3% shows obviously higher values than SA-PDI. The estimated spectral-averaged specific extinction coefficients  $\beta^*$  of SA-PDI and Ag@AgCl/PDI-3% in the region from 400 to 800 nm are 441.7 m<sup>2</sup> kg<sup>-1</sup> and 941.4 m<sup>2</sup> kg<sup>-1</sup>, respectively. Based on the obtained  $\beta^*$ , the length for the extinction of the light inside the reactor  $L$  (0.068 m) and catalyst mass concentration  $C_{\text{cat}}$  (0.2 g/L), the optical thickness  $\tau$  of SA-PDI and Ag@AgCl/PDI-3% suspensions in the reactor calculated by the equation of  $\tau = \beta^* C_{\text{cat}} L$  are 6.0 and 12.8, respectively. Since the optical thickness  $\tau$  in the reactor of Ag@AgCl/PDI-3% is nearly 2.1 times as that of SA-PDI, we have increased the mass concentration of SA-PDI to 2.1 times as that of Ag@AgCl/PDI-3% to make a fair comparison between SA-PDI and Ag@AgCl/PDI-3% photocatalysts. As shown in Figs. S12 and 5b, Ag@AgCl/PDI-3% (10 mg) still possesses higher  $k$  values for phenol, BPA, SDM and OFX degradation under visible light, which are about 5.3, 2.2, 2.9 and 3.5 times as those of SA-PDI (21 mg), respectively, indicating that Ag@AgCl/PDI-3% can exhibit significantly enhanced photocatalytic performance even at equal optical thickness  $\tau$  as SA-PDI.

### 3.2.2. Photocatalytic inactivation of ARB and ARGs

Sulfonamide ARB and ARGs are considered to be one kind of the most

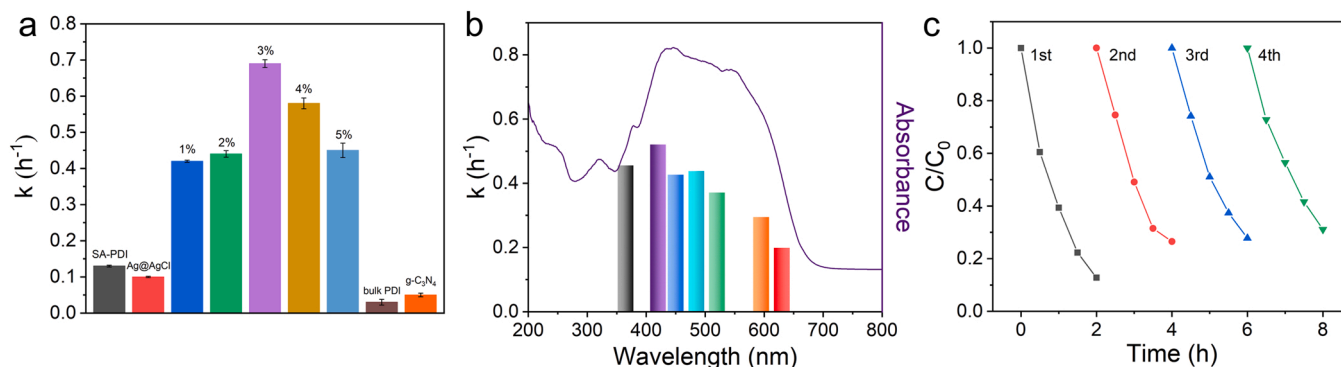


**Fig. 4.** (a) The apparent rate constants ( $k$ ) for phenol photodegradation of SA-PDI, Ag@AgCl, Ag@AgCl/PDI, bulk PDI and g-C<sub>3</sub>N<sub>4</sub> under visible light calculated via the pseudo-first-order kinetic fitting. (b) Photocatalytic activities of Ag@AgCl/PDI-3% at different wavelengths for degradation of phenol. (c) The stability of Ag@AgCl/PDI-3% for phenol degradation under visible light.

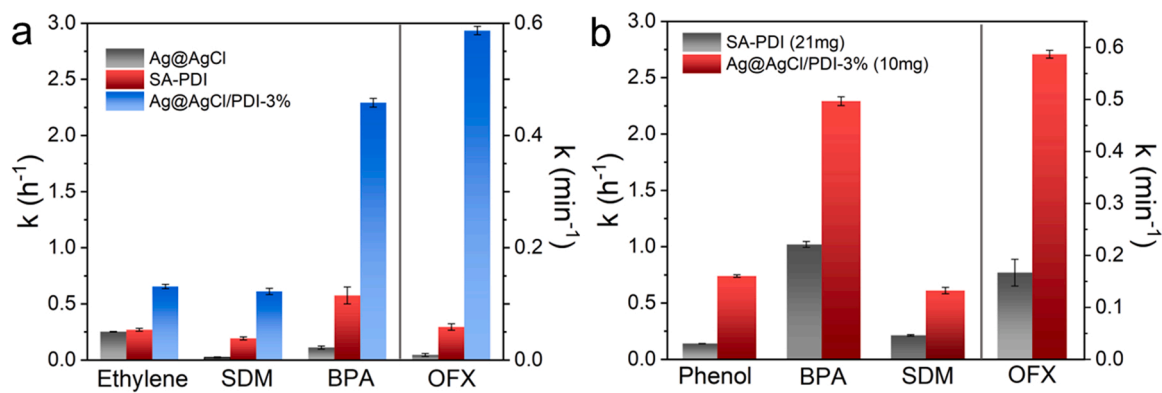


**Fig. 5.** (a) The  $k$  values for different pollutants degradation of SA-PDI, Ag@AgCl and Ag@AgCl/PDI-3% under visible light. (b) The  $k$  values for different pollutants degradation of SA-PDI and Ag@AgCl/PDI-3% at equal optical thickness  $\tau$  under visible light.

dominant ARB and ARGs in the water environment, which have high detection rates in surface water, underground water, culture wastewater, medical wastewater and even drinking water [61–63]. Herein, the advantage of Ag@AgCl/PDI in disinfection application was further demonstrated by the antibacterial experiments towards sulfonamide ARB. As shown in Fig. 6a, few bacteria can be inactivated in the light control group, suggesting that visible light has no bactericidal effect on ARB. In the dark control group, Ag@AgCl/PDI-3% itself shows a certain effectivity in sterilizing sulfonamide ARB without the irradiation due to the excellent antibacterial ability of the loaded AgNPs. In contrast, the photocatalytic sterilization efficiency of Ag@AgCl/PDI-3% towards sulfonamide ARB after 2 h of visible light irradiation is almost 100%, which is significantly higher than that of SA-PDI (49.4%). In addition, Ag@AgCl also exhibits similar excellent sterilization efficiency as Ag@AgCl/PDI-3%, which is attributed to its high content of AgNPs. It is noteworthy that although Ag@AgCl/PDI-3% only decorate a relatively low amount of Ag@AgCl, it still achieves a remarkable antibacterial ability, which should mainly ascribe to the synergistic interaction between Ag@AgCl and SA-PDI. Fig. S13 compares the number of sulfonamide ARB colonies on LB agar plates in different groups during the antibacterial process, which can visually demonstrate the synergistic antibacterial performance of Ag@AgCl/PDI system. The potential of Ag@AgCl/PDI photocatalyst applied in the inactivation of ARGs was investigated by using sulfonamide ARGs (*sul1*) as the target. According to the standard curve shown in Fig. S14, the absolute abundance of *sul1* genes in the water sample treated with SA-PDI decreases from the initial  $10^{6.5}$  copies/mL to  $10^{6.2}$  copies/mL after 8 h of visible light irradiation

with a reduction of 0.3 lg, indicating that SA-PDI has a certain inactivation effect on *sul1* genes. In contrast, the absolute abundance of *sul1* genes in the water sample treated with Ag@AgCl/PDI-3% decreases from the initial  $10^{6.5}$  copies/mL to  $10^{4.1}$  copies/mL with a reduction of 2.4 lg. The removal rate of Ag@AgCl/PDI-3% towards *sul1* genes reaches 99.6%, which is about twice as high as that of SA-PDI (49.9%) (Fig. 6b).

Based on the discussions above, compared with SA-PDI, Ag@AgCl/PDI possesses significantly enhanced photocatalytic oxidation performance by loading Ag@AgCl, which can effectively remove organic pollutants, ARB and ARGs. Thus, Ag@AgCl/PDI composite photocatalyst has a promising application prospect in water treatment.

### 3.3. Mechanism of highly efficient photocatalytic performance of Ag@AgCl/PDI composite

#### 3.3.1. Photogenerated carriers behavior analysis

The photogenerated carriers behavior was investigated by photoelectrochemical tests to clarify the effect of charge transfer efficiency on the enhanced photocatalytic performance of Ag@AgCl/PDI composites. As shown in Fig. 7a, the photocurrent response of Ag@AgCl/PDI-3% under visible light irradiation is about 1.9 times higher than that of SA-PDI, indicating that the photogenerated carriers separation has been enormously accelerated due to the formation of heterogeneous interface between Ag@AgCl and SA-PDI. Besides, the photocurrents of SA-PDI and Ag@AgCl/PDI-3% composite firstly increase rapidly and subsequently decrease slowly under chopped illumination, which could be

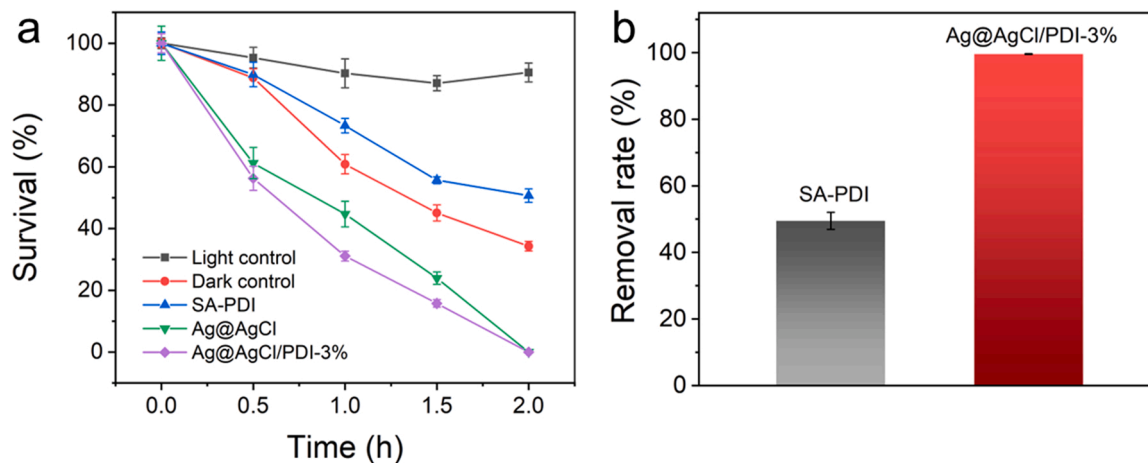


**Fig. 6.** (a) Visible-light-induced photocatalytic disinfection performance against sulfonamide ARB over Ag@AgCl, SA-PDI and Ag@AgCl/PDI-3%. (b) Comparison of the removal rate of SA-PDI and Ag@AgCl/PDI-3% towards *sul1* genes.



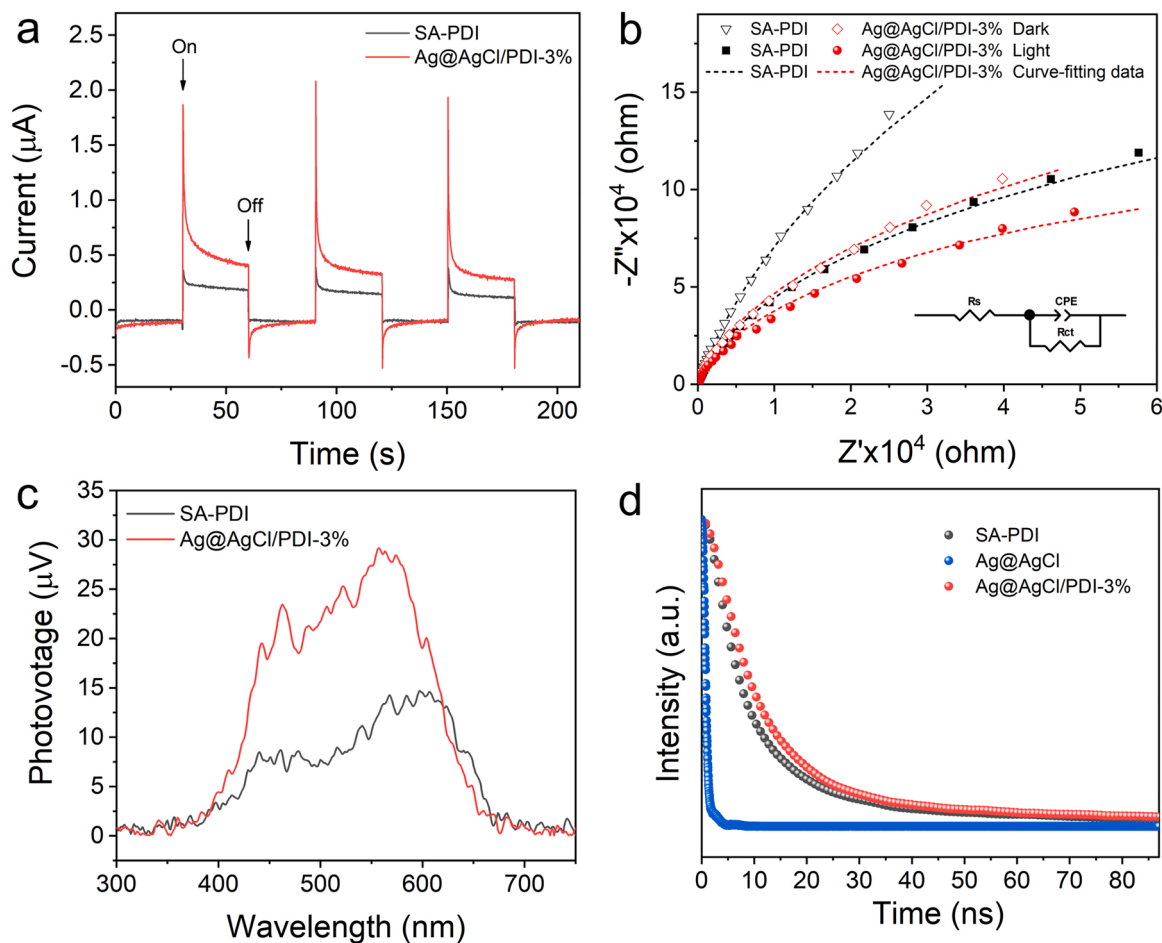


**Fig. 7.** (a) Photocurrent response curves under chopped illumination. (b) EIS Nyquist plots without and with visible light irradiation with the fitted equivalent circuit in the inset. (c) SPV spectroscopy, and (d) Time-resolved fluorescence decay spectra of Ag@AgCl, SA-PDI and Ag@AgCl/PDI-3%.

attributed to the charge and discharge of the electric double layer during the electrode polarization process [64]. As observed in Fig. 7b, both SA-PDI and Ag@AgCl/PDI-3% exhibit semicircular electrochemical impedance spectroscopy (EIS) Nyquist plots, and the radii of Ag@AgCl/PDI-3% composite under light and dark conditions are both smaller than those of SA-PDI. Since smaller arc radius of Nyquist plots is corresponding to lower transfer resistance of interfacial electrons, Ag@AgCl/PDI-3% should have lower recombination rate of photo-generated  $e^-h^+$  pairs [65]. According to the equivalent circuit and the fitted parameters listed in Table S3, the charge transfer resistance ( $R_{ct}$ ) of Ag@AgCl/PDI-3% (230.80 k $\Omega$ ) is much smaller than SA-PDI (346.5 k $\Omega$ ) under visible light irradiation, further evidencing that the loading of Ag@AgCl endows the composite a better charge transfer efficiency to promote the photocatalytic reaction. In addition, the SPV signal of Ag@AgCl/PDI-3% is significantly stronger than that of SA-PDI in the range of 400–600 nm (Fig. 7c), indicating that Ag@AgCl/PDI-3% has reinforced charge separation efficiency. This might be due to the fact that AgNPs in the heterostructure can act as a bridge of charge transportation and thus facilitate the migration of electrons and holes in opposite directions.

The charge transfer kinetics of Ag@AgCl/PDI was further verified by fluorescence spectroscopy [66]. As shown in Fig. S15, Ag@AgCl shows no fluorescence signal, while PDI exhibits an emission peak at about 670 nm under the excitation wavelength of 468 nm. Compared to SA-PDI, Ag@AgCl/PDI-3% exhibits a red-shifted emission peak at 680 nm with weaker intensity, demonstrating the presence of heterojunction interface could efficiently redistribute the charge density and thus suppress the charge recombination in the composite system [43].

Furthermore, the fluorescence lifetime of Ag@AgCl, SA-PDI and Ag@AgCl/PDI-3% were tested using time-resolved fluorescence decay spectroscopy. As shown in Fig. 7d, the fluorescence intensities of Ag@AgCl, SA-PDI and Ag@AgCl/PDI-3% all decay exponentially. Based on the bi-exponential fitting results (Table S4), the average fluorescence lifetimes ( $\tau_{ave}$ ) of Ag@AgCl, SA-PDI and Ag@AgCl/PDI-3% are calculated to be 1.37, 7.80 and 10.29 ns, respectively. Thus, the lifetime of charge carriers involved in the photocatalytic process has been extended after the loading of Ag@AgCl, which improves the photocatalytic performance of Ag@AgCl/PDI composite.

To acquire an insight into the generation and transfer mechanism of photogenerated carriers in Ag@AgCl/PDI-3% heterojunction, femto-second transient absorption spectroscopy (TAS) was conducted under 550 nm excitation to record the real-time photogenerated charge dynamics. As depicted in Fig. 8a and b, the negative ground-state bleaching (GB) peaks appear at 511 nm and 545 nm, accompanied with the positive excited state absorption (ESA) peak from 550 to 650 nm corresponding to the electron transition of singlet  $S_1 \rightarrow S_N$  [67]. The absorption peaks of  $PDI^+$  at 470 nm and  $PDI^-$  at 593 nm can also be found. Compared with SA-PDI, Ag@AgCl/PDI-3% shows quicker disappearance of GB peak at 511 nm and the weakening peaks of  $PDI^+$  and  $PDI^-$ . Upon the visible light excitation, the excited process involves in the transformation of PDI state from aggregate to intermolecular charge transfer state, further to polarized exciton state, and finally to PDI free carriers [68]. Theoretically, the kinetics of  $PDI^-$  peaks at 593 nm could offer the information about the lifetime of charge recombination ( $\tau_{CR}$ ) [69]. The time profiles of TAS probed at 593 nm were fitted to estimate the decay kinetics of photogenerated carriers

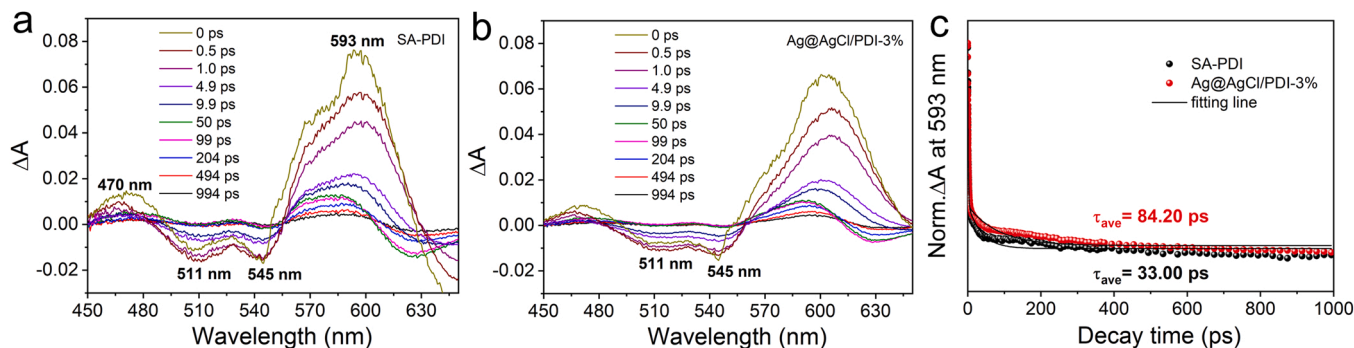


Fig. 8. Transient absorption spectra for (a) SA-PDI and (b) Ag@AgCl/PDI-3%. (c) Time profiles of normalized transient absorption at 593 nm.

(Fig. 8c). As listed in Table S5,  $\tau_{CR}$  of Ag@AgCl/PDI-3% (84.20 ps) is 2.6 times as that of SA-PDI (33.00 ps). Thus, Ag@AgCl/PDI shows slower charge recombination rate, leading to the remarkably enhanced photocatalytic performance in comparison with SA-PDI.

DFT calculations were performed to further clarify the Z-scheme mechanism of electrons transfer process in Ag@AgCl/PDI photocatalytic system. As shown in Fig. 9a, b and c, the work functions calculated by subtracting the Fermi level ( $E_F$ ) values from the Vacuum level ( $E_V$ ) values of SA-PDI, Ag and AgCl are 2.50, 4.54 and 5.31 eV, respectively [70–72]. It is clear that the  $E_F$  values are in order of SA-PDI < Ag < AgCl. As shown in Fig. 9d, after contacting, electrons can spontaneously transfer from SA-PDI through Ag to AgCl until the  $E_F$  values of three components reach the same level [73]. The migration of electrons leads to the decrease of electronic density in SA-PDI and the increase in AgCl, which make the surface of SA-PDI positively charged and the surface of AgCl negatively charged. The charge redistribution results in the

formation of built-in electric field and band bending at the hetero-junction interface, which can further facilitate the free electrons outflow from the downward bent band of AgCl and inflow to the upward bent band of SA-PDI via Ag under light irradiation [74]. Thus, the Ag-bridged Z-scheme electron transfer mechanism of Ag@AgCl/PDI heterojunction is proposed in Fig. 9e based on the Fermi level and built-in electric field.

### 3.3.2. Active species in photocatalytic reactions

The identification of active species produced by Ag@AgCl/PDI composite and their contributions to the photocatalytic process were investigated by radical trapping experiments and electron spin resonance (ESR) analysis. Ammonium oxalate (AO), p-benzoquinone (p-BQ), isopropanol (IPA) and furfuryl alcohol (FFA) were added to capture photogenerated holes ( $h^+$ ), superoxide radicals ( $\bullet O_2^-$ ), hydroxyl radicals ( $\bullet OH$ ) and singlet oxygen ( $^1O_2$ ) in the phenol degradation tests, respectively. As shown in Fig. 10a, the addition of p-BQ significantly

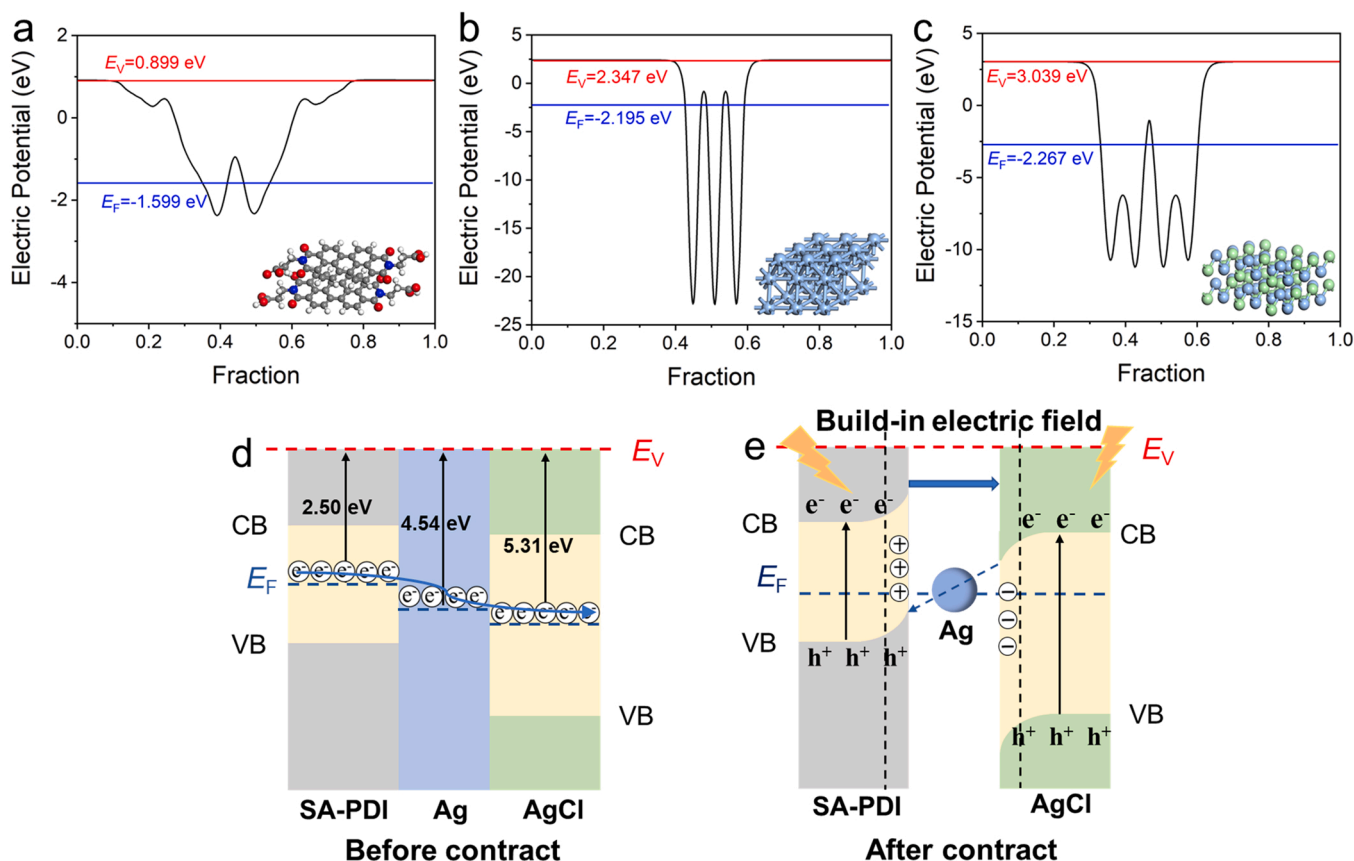
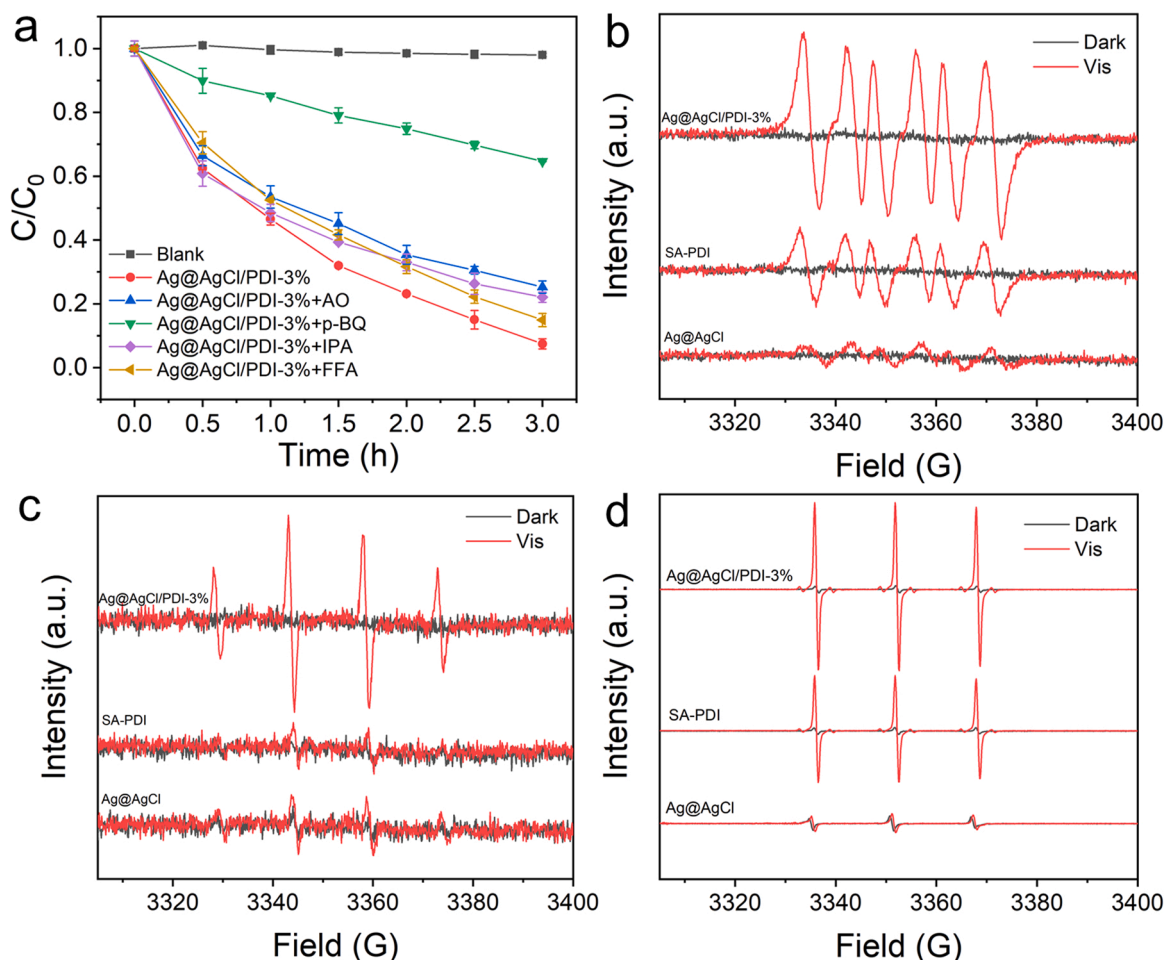


Fig. 9. Calculated work functions of (a) SA-PDI ( $\pi$ - $\pi$  stacking plane), (b) Ag (111) and (c) AgCl (220). (d-e) Schematic diagram of the charge transfer process in Ag@AgCl/PDI.



**Fig. 10.** (a) The influence of different active species scavengers on the phenol degradation activity of Ag@AgCl/PDI-3% under visible light. ESR spectra of Ag@AgCl, SA-PDI and Ag@AgCl/PDI-3% without and with visible light irradiation for the detection of (b)  $\bullet O_2$ , (c)  $\bullet OH$  and (d)  $^1O_2$ .

inhibits the degradation efficiency of Ag@AgCl/PDI-3%, and the addition of AO, FFA or IPA also reduces the degradation activity to some extent. We fitted the pseudo-first-order kinetic model in the degradation reaction with the addition of scavenger (Fig. S16a) and used the  $k$  values to calculate the contribution ratio of each active species [75]. As shown in Fig. S16b, it can be found that the contribution ratio of each active species is in order of  $\bullet O_2 > h^+ > \bullet OH > ^1O_2$ , indicating that  $\bullet O_2$  is the main active species while  $h^+$ ,  $\bullet OH$  and  $^1O_2$  also participate in the photocatalytic reaction.

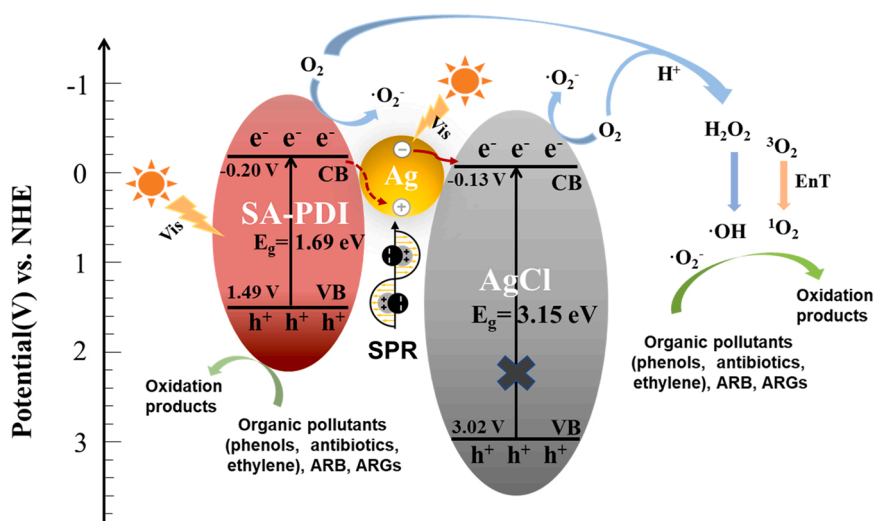
In the ESR analysis, 5,5-dimethyl-1-pyrroline-N-oxide (DMPO) was used as the spin probe to detect  $\bullet O_2$  in methanol and  $\bullet OH$  in  $H_2O$ , while 2,2,6,6-tetramethyl-4-piperidone (TEMP) and 2,2,6,6-tetramethylpiperidine-1-oxygen radical (TEMPO) were used as spin probes to detect  $^1O_2$  and electrons ( $e^-$ ) in  $H_2O$ , respectively [76]. As shown in Fig. 10b and c, the signal intensities of DMPO- $\bullet O_2$  and DMPO- $\bullet OH$  of Ag@AgCl/PDI-3% are much stronger than those of SA-PDI and AgCl under visible light, suggesting there are larger amounts of  $\bullet O_2$  and  $\bullet OH$  generated in the composite system. Besides, the  $\bullet O_2$  signal is more pronounced than the  $\bullet OH$  signal, further confirming that  $\bullet O_2$  is the main contributing active species in the photocatalytic process of Ag@AgCl/PDI-3%. As shown in Fig. 10d, Ag@AgCl is almost unable to produce  $^1O_2$ , while both SA-PDI and Ag@AgCl/PDI-3% show a 1:1:1 triplet signal of  $^1O_2$  under visible light. The signal intensity of Ag@AgCl/PDI-3% is higher than that of SA-PDI, indicating the more production of  $^1O_2$ . As shown in Fig. S17, all three samples show weakened triple ESR signals upon visible light irradiation. Moreover, the ESR signal of Ag@AgCl/PDI-3% decreases more significantly in comparison

with Ag@AgCl and SA-PDI, suggesting that more photogenerated  $e^-$  could participate in the photocatalytic reaction of Ag@AgCl/PDI to produce larger numbers of  $\bullet O_2$  and  $H_2O_2$  via the reduction of  $O_2$  [77, 78]. The above results demonstrate that the loading of Ag@AgCl could remarkably increase the amount of active species ( $\bullet O_2$ ,  $^1O_2$ ,  $h^+$  and  $\bullet OH$ ) produced during the photocatalytic process, resulting in the significantly enhanced photocatalytic oxidation performance of Ag@AgCl/PDI composite.

### 3.3.3. Carriers separation and photocatalytic process

Based on the aforementioned results, we propose the mechanism of carriers separation and photocatalytic process under visible light in Ag@AgCl/PDI composite system. As shown in Scheme 2, SA-PDI photocatalyst can be excited by visible light with a band gap energy of 1.69 eV. In addition, the SPR effect of AgNPs can further improve the light absorption ability, leading to the generation of more photo-generated carriers participated in photocatalytic process of Ag@AgCl/PDI composite. Meanwhile, AgCl has no spectral response in visible light region with a wide band gap of 3.15 eV, while AgNPs can be excited under visible light and generate  $e^-$  based on the SPR effect. After the loading of Ag@AgCl on the surface of SA-PDI, on one hand, the SPR-effect excited  $e^-$  can transport from Ag to the surface of AgCl through the heterogeneous interface due to the Schottky barrier formed by  $Ag^0$ ; on the other hand, the remaining positive charge species existed in the region of Ag could effectively capture the photogenerated  $e^-$  on the CB of SA-PDI to accelerate the carriers separation efficiency in SA-PDI, while the left photogenerated  $h^+$  on the VB of SA-PDI to oxidize organic





**Scheme 2.** The schematic diagram of proposed mechanism of carriers separation and photocatalytic process under visible light in Ag@AgCl/PDI composite system.

pollutants, ARB and ARGs. Therefore, a plasmonic Ag@AgCl/PDI photocatalyst system is constructed with accelerated carriers separation efficiency and inhibited recombination rate of photogenerated  $e^-h^+$  pairs. During the photocatalytic process, the accumulated  $e^-$  on the CB of SA-PDI and AgCl are able to react with the adsorbed  $O_2$  to produce more  $\bullet O_2^-$ , and  $^3O_2$  can be converted to  $^1O_2$  through the energy transfer process [64,79]. Besides, although  $h^+$  on the VB of SA-PDI cannot oxidize  $OH^-$  to  $\bullet OH$  due to the less positive  $E_{VB}$  than  $E^0(OH^-/\bullet OH)$  (1.99 V vs. NHE), there are more production of  $H_2O_2$  via the two-electron reduction reaction between  $O_2$  and  $H^+$ , which can subsequently convert to  $\bullet OH$  and further improve the oxidation capacity of the composite system [80]. Under the combined effect of  $\bullet O_2^-$ ,  $^1O_2$ ,  $h^+$  and  $\bullet OH$ , Ag@AgCl/PDI can thoroughly mineralize organic pollutants (phenols, antibiotics and ethylene) and effectively inactivate sulfonamide ARB and ARGs. Therefore, the plasmonic Z-scheme heterojunction structure endows Ag@AgCl/PDI photocatalyst with higher solar light utilization, faster carriers separation efficiency and stronger oxidation capacity, which remarkably enhance its photocatalytic performance for the removal of organic pollutants, ARB and ARGs.

#### 4. Conclusion

In summary, a plasmonic Z-scheme Ag@AgCl/PDI photocatalyst was fabricated by in-situ deposition-photoreduction method. Compared with SA-PDI, Ag@AgCl/PDI exhibited more excellent photocatalytic oxidation performance under visible light for the elimination of organic pollutants, ARB and ARGs, which could be mainly due to the following three reasons: (1) the SPR effect of AgNPs could improve the solar light utilization of the composite to generate more charge carriers participated in the photocatalytic reaction; (2) AgNPs could act as electron sinks to effectively capture the  $e^-$  on the CB of SA-PDI, while the Schottky barrier formed by  $Ag^0$  could promote the SPR-excited  $e^-$  to migrate from Ag to AgCl, further accelerating the carriers separation efficiency; (3) more active species ( $\bullet O_2^-$ ,  $^1O_2$ ,  $h^+$  and  $\bullet OH$ ) could be produced in the photocatalytic process to enhance the oxidation capacity of Ag@AgCl/PDI. This work not only provides a new perspective for designing highly efficient plasmonic Z-scheme photocatalysts, but also expands the application prospects of PDI-based materials in the fields of environmental purification and food safety.

#### CRediT authorship contribution statement

**Xue Chen:** Methodology, Validation, Formal analysis, Investigation, Data curation, Writing – original draft, Visualization. **Zhouping Wang:**

Resources, Supervision, Funding acquisition. **Xuancheng Shen:** Formal analysis, Data curation. **Yan Zhang:** Resources, Methodology. **Yang Lou:** Resources. **Chengsi Pan:** Resources. **Yongfa Zhu:** Resources. **Jing Xu:** Conceptualization, Methodology, Validation, Investigation, Resources, Writing – review & editing, Visualization, Supervision, Project administration, Funding acquisition.

#### Declaration of Competing Interest

The authors declare that they have no known competing financial interests or personal relationships that could have appeared to influence the work reported in this paper.

#### Data Availability

Data will be made available on request.

#### Acknowledgements

This work was supported by the Natural Science Foundation of Jiangsu Province (BK20221541, BK20211239 and BK20201345), Jiangsu Agriculture Science and Technology Innovation Fund (CX(20)3108), National Natural Science Foundation of China (21707052, 31871881, 21908079 and 22172065), Fundamental Research Funds for the Central Universities (JUSRP11905). The femtosecond transient absorption measurements were conducted at Yu-Xiang Weng's laboratory at Institute of Physics CAS, and we were grateful to Zhuan Wang for her help of taking TAS data.

#### Appendix A. Supporting information

Supplementary data associated with this article can be found in the online version at doi:10.1016/j.apcatb.2022.122220.

#### References

- [1] X.L. Jin, L.Q. Ye, H.Q. Xie, G. Chen, Bismuth-rich bismuth oxyhalides for environmental and energy photocatalysis, *Coord. Chem. Rev.* 349 (2017) 84–101.
- [2] S.Y. Lee, B.N. Kim, J.H. Han, S.T. Chang, Y.W. Choi, Y.H. Kim, J. Min, Treatment of phenol-contaminated soil by *Corynebacterium glutamicum* and toxicity removal evaluation, *J. Hazard. Mater.* 182 (2010) 937–940.
- [3] J.X. Zhang, M.L. Xie, H.Y. Zhao, L.R. Zhang, G.F. Wei, G.H. Zhao, Preferential and efficient degradation of phenolic pollutants with cooperative hydrogen-bond interactions in photocatalytic process, *Chemosphere* 269 (2021), 129404.
- [4] C.T. Guan, J. Jiang, S.Y. Pang, C.W. Luo, Y. Yang, J. Ma, J. Yu, X. Zhao, Effect of iodide on transformation of phenolic compounds by nonradical activation of

- peroxydisulfate in the presence of carbon nanotube: Kinetics, impacting factors, and formation of iodinated aromatic products, *Chemosphere* 208 (2018) 559–568.
- [5] M.T. Guo, X.B. Tian, Impacts on antibiotic-resistant bacteria and their horizontal gene transfer by graphene-based  $\text{TiO}_2/\text{Ag}$  composite photocatalysts under solar irradiation, *J. Hazard. Mater.* 380 (2019), 120877.
  - [6] O. Baaloudj, I. Assadi, N. Nasrallah, A. El Jery, L. Khezami, A.A. Assadi, Simultaneous removal of antibiotics and inactivation of antibiotic-resistant bacteria by photocatalysis: a review, *J. Water Process Eng.* 42 (2021), 102089.
  - [7] S.N. Li, C.F. Zhang, F.X. Li, T. Hua, Q.X. Zhou, S.H. Ho, Technologies towards antibiotic resistance genes (ARGs) removal from aquatic environment: a critical review, *J. Hazard. Mater.* 411 (2021), 125148.
  - [8] Z. Zhou, Z. Shen, Z. Cheng, G. Zhang, M. Li, Y. Li, S. Zhan, J.C. Crittenden, Mechanistic insights for efficient inactivation of antibiotic resistance genes: a synergistic interfacial adsorption and photocatalytic-oxidation process, *Sci. Bull.* 65 (2020) 2107–2119.
  - [9] M.E. Saltveit, Effect of ethylene on quality of fresh fruits and vegetables, *Postharvest Biol. Technol.* 15 (1999) 279–292.
  - [10] S.H. Huo, W.T. Gao, P.X. Zhou, Z.P. Deng, Z.G. Han, X.T. Cui, X.Q. Lu, Magnetic porous carbon composites for rapid and highly efficient degradation of organic pollutants in water, *Adv. Powder Mater.* 1 (2022), 100028.
  - [11] X.N. Wang, F.L. Wang, Y.H. Sang, H. Liu, Full-spectrum solar-light-activated photocatalysts for light-chemical energy conversion, *Adv. Energy Mater.* 7 (2017), 1700473.
  - [12] X.B. Chen, S.H. Shen, L.J. Guo, S.S. Mao, Semiconductor-based photocatalytic hydrogen generation, *Chem. Rev.* 110 (2010) 6503–6570.
  - [13] Z.H. Wu, J.F. Jing, K.F. Zhang, W.L. Li, J. Yang, J. Shen, S.M. Zhang, K.Q. Xu, S. Y. Zhang, Y.F. Zhu, Epitaxial  $\text{BiPb}_2\text{O}_{14}$  layer on  $\text{BiOI}$  nanosheets enhancing the photocatalytic degradation of phenol via interfacial internal-electric-field, *Appl. Catal. B Environ.* 307 (2022), 121153.
  - [14] G. Afreen, M. Shoaib, S. Upadhyaya, Effectiveness of reactive oxygen species generated from  $\text{rGO}/\text{CdS}$  QD heterostructure for photodegradation and disinfection of pollutants in waste water, *Mater. Sci. Eng. C -Mater. Biol. Appl.* 108 (2020), 110372.
  - [15] S. Das, A.J. Misra, A.P.H. Rahman, B. Das, R. Jayabalan, A.J. Tamhankar, A. Mishra, C.S. Lundborg, S.K. Tripathy,  $\text{Ag}@\text{SnO}_2/\text{ZnO}$  core-shell nanocomposites assisted solar-photocatalysis downregulates multidrug resistance in *Bacillus* sp.: A catalytic approach to impede antibiotic resistance, *Appl. Catal. B Environ.* 259 (2019), 118065.
  - [16] D. Saha, M.C. Visconti, M.M. Desipio, R. Thorpe, Inactivation of antibiotic resistance gene by ternary nanocomposites of carbon nitride, reduced graphene oxide and iron oxide under visible light, *Chem. Eng. J.* 382 (2020), 122857.
  - [17] L.W. Wang, X. Zhang, X. Yu, E.N. Gao, Z.Y. Shen, X.L. Zhang, S.G. Ge, J. Liu, Z. J. Gu, C.Y. Chen, An all-organic semiconductor  $\text{C}_3\text{N}_4/\text{PDINH}$  heterostructure with advanced antibacterial photocatalytic therapy activity, *Adv. Mater.* 31 (2019), 1901965.
  - [18] X.J. Bai, L.L. Guo, T.Q. Jia, D.R. Hao, C. Wang, H.Y. Li, R.L. Zong, Perylene diimide growth on both sides of carbon nanotubes for remarkably boosted photocatalytic degradation of diclofenac, *J. Hazard. Mater.* 435 (2022), 128992.
  - [19] Q.Y. Ji, X.Y. Cheng, Y.J. Wu, W.M. Xiang, H. He, Z. Xu, C.M. Xu, C.D. Qi, S.Y. Li, L. M. Zhang, S.G. Yang, Visible light absorption by perylene diimide for synergistic persulfate activation towards efficient photodegradation of bisphenol A, *Appl. Catal. B Environ.* 282 (2021), 119579.
  - [20] Q.C. Zhang, L. Jiang, J. Wang, Y.F. Zhu, Y.J. Pu, W.D. Dai, Photocatalytic degradation of tetracycline antibiotics using three-dimensional network structure perylene diimide supramolecular organic photocatalyst under visible-light irradiation, *Appl. Catal. B Environ.* 277 (2020), 119122.
  - [21] D. Liu, J. Wang, X.J. Bai, R.L. Zong, Y.F. Zhu, Self-assembled PDINH supramolecular system for photocatalysis under visible light, *Adv. Mater.* 28 (2016) 7284–7290.
  - [22] J. Yang, H. Miao, W.L. Li, H.Q. Li, Y.F. Zhu, Designed synthesis of a  $\text{p-Ag}_2\text{S}/\text{n-PDI}$  self-assembled supramolecular heterojunction for enhanced full-spectrum photocatalytic activity, *J. Mater. Chem. A* 7 (2019) 6482–6490.
  - [23] S. Patnaik, D.P. Sahoo, K. Parida, An overview on Ag modified  $\text{g-C}_3\text{N}_4$  based nanostructured materials for energy and environmental applications, *Renew. Sust. Energ. Rev.* 82 (2018) 1297–1312.
  - [24] H. Miao, J. Yang, Y.X. Wei, W.L. Li, Y.F. Zhu, Visible-light photocatalysis of PDI nanowires enhanced by plasmonic effect of the gold nanoparticles, *Appl. Catal. B Environ.* 239 (2018) 61–67.
  - [25] Y.Z. Hong, Y.H. Jiang, C.S. Li, W.Q. Fan, X. Yan, M. Yan, W.D. Shi, In-situ synthesis of direct solid-state Z-scheme  $\text{V}_2\text{O}_5/\text{g-C}_3\text{N}_4$  heterojunctions with enhanced visible light efficiency in photocatalytic degradation of pollutants, *Appl. Catal. B Environ.* 180 (2016) 663–673.
  - [26] X. Xie, S.B. Wang, Y.J. Zhang, J. Ding, Y.G. Liu, Q.S. Yan, S.Y. Lu, B.J. Li, Y.S. Liu, Q. Cai, Facile construction for new core-shell Z-scheme photocatalyst  $\text{GO}/\text{AgI}/\text{Bi}_2\text{O}_3$  with enhanced visible-light photocatalytic activity, *J. Colloid Interface Sci.* 581 (2021) 148–158.
  - [27] P.F. Hu, Y.L. Cao, A new chemical route to a hybrid nanostructure: Room-temperature solid-state reaction synthesis of  $\text{Ag}@\text{AgCl}$  with efficient photocatalysis, *Dalton Trans.* 41 (2012) 8908–8912.
  - [28] H.Y. Li, Y.J. Sun, B. Cai, S.Y. Gan, D.X. Han, L. Niu, T.S. Wu, Hierarchically Z-scheme photocatalyst of  $\text{Ag}@\text{AgCl}$  decorated on  $\text{BiVO}_4$  (040) with enhancing photoelectrochemical and photocatalytic performance, *Appl. Catal. B Environ.* 170 (2015) 206–214.
  - [29] F.H. Mu, C.X. Liu, Y. Xie, S.J. Zhou, B.L. Dai, D.H. Xia, H.B. Huang, W. Zhao, C. Sun, Y. Kong, D.Y.C. Leung, Metal-organic framework-derived rodlike  $\text{AgCl}/\text{Ag}/\text{In}_2\text{O}_3$ : A plasmonic Z-scheme visible light photocatalyst, *Chem. Eng. J.* 415 (2021), 129010.
  - [30] J.F. Guo, B.W. Ma, A.Y. Yin, K.N. Fan, W.L. Dai, Highly stable and efficient  $\text{Ag}/\text{AgCl}/\text{TiO}_2$  photocatalyst: Preparation, characterization, and application in the treatment of aqueous hazardous pollutants, *J. Hazard. Mater.* 211 (2012) 77–82.
  - [31] S.X. Zhong, Y.M. Xi, Q. Chen, J.R. Chen, S. Bai, Bridge engineering in photocatalysis and photoelectrocatalysis, *Nanoscale* 12 (2020) 5764–5791.
  - [32] Q.X. Liu, C.M. Zeng, L.H. Ai, Z. Hao, J. Jiang, Boosting visible light photoreactivity of photoactive metal-organic framework: Designed plasmonic Z-scheme  $\text{Ag}/\text{AgCl}/\text{MIL-53-Fe}$ , *Appl. Catal. B Environ.* 224 (2018) 38–45.
  - [33] P.P. Li, H.X. Wu, A. Dong,  $\text{Ag}/\text{AgX}$  nanostructures serving as antibacterial agents: achievements and challenges, *Rare Met* 41 (2022) 519–539.
  - [34] N.X. Yu, H.L. Peng, L. Qiu, R.H. Wang, C.J. Jiang, T.M. Cai, Y. Sun, Y.B. Li, H. Xiong, New pectin-induced green fabrication of  $\text{Ag}@\text{AgCl}/\text{ZnO}$  nanocomposites for visible-light triggered antibacterial activity, *Int. J. Biol. Macromol.* 141 (2019) 207–217.
  - [35] Y.Z. Zhou, R. Chen, T.T. He, K. Xu, D. Du, N. Zhao, X.N. Cheng, J. Yang, H.F. Shi, Y. H. Lin, Biomedical potential of ultrafine  $\text{Ag}/\text{AgCl}$  nanoparticles coated on graphene with special reference to antimicrobial performances and burn wound healing, *ACS Appl. Mater. Interfaces* 8 (2016) 15067–15075.
  - [36] Y. Luo, D.Q. Mao, M. Rysz, D.X. Zhou, H.J. Zhang, L. Xu, P.J.J. Alvarez, Trends in antibiotic resistance genes occurrence in the Haihe River, China, *Environ. Sci. Technol.* 44 (2010) 7220–7225.
  - [37] M. Tamminen, A. Karkman, A. Lohmus, W.I. Muziasari, H. Takasu, S. Wada, S. Suzuki, M. Virta, Tetracycline resistance genes persist at aquaculture farms in the absence of selection pressure, *Environ. Sci. Technol.* 45 (2011) 386–391.
  - [38] J. Wang, W. Shi, D. Liu, Z.J. Zhang, Y.F. Zhu, D. Wang, Supramolecular organic nanofibers with highly efficient and stable visible light photooxidation performance, *Appl. Catal. B Environ.* 202 (2017) 289–297.
  - [39] X. Yu, J.L. Huang, J.J. Zhao, S.F. Liu, D.D. Xiang, Y.T. Tang, J. Li, Q.H. Guo, X. Q. Ma, J.W. Zhao, Efficient visible light photocatalytic antibiotic elimination performance induced by nanostructured  $\text{Ag}/\text{AgCl}/\text{Ti}^{3+}/\text{TiO}_2$  mesocrystals, *Chem. Eng. J.* 403 (2021), 126359.
  - [40] S.B. Yang, D.B. Xu, B.Y. Chen, B.F. Luo, W.D. Shi, In-situ synthesis of a plasmonic  $\text{Ag}/\text{AgCl}/\text{Ag}_2\text{O}$  heterostructures for degradation of ciprofloxacin, *Appl. Catal. B Environ.* 204 (2017) 602–610.
  - [41] J.Q. Gong, W.W. Zhang, T. Sen, Y.C. Yu, Y.C. Liu, J.L. Zhang, L.Z. Wang, Metal-organic framework MIL-101(Fe) nanoparticles decorated with Ag nanoparticles for regulating the photocatalytic phenol oxidation pathway for  $\text{Cr(VI)}$  reduction, *ACS Appl. Nano Mater.* 4 (2021) 4513–4521.
  - [42] G.D. Fan, J.J. Zhan, J. Luo, J.Y. Lin, F.S. Qu, B.H. Du, Y.F. You, Z.S. Yan, Fabrication of heterostructured  $\text{Ag}/\text{AgCl}/\text{g-C}_3\text{N}_4/\text{UiO-66}(\text{NH}_2)$  nanocomposite for efficient photocatalytic inactivation of *Microcystis aeruginosa* under visible light, *J. Hazard. Mater.* 404 (2021), 124062.
  - [43] W.D. Zhang, X.G. Dong, Y. Liang, Y.J. Sun, F. Dong,  $\text{Ag}/\text{AgCl}$  nanoparticles assembled on  $\text{BiOCl}/\text{Bi}_{12}\text{O}_{17}\text{Cl}_2$  nanosheets: Enhanced plasmonic visible light photocatalysis and in situ DRIFTS investigation, *Appl. Surf. Sci.* 455 (2018) 236–243.
  - [44] S.F. Yang, C.G. Niu, D.W. Huang, H. Zhang, C. Lianga, G.M. Zeng,  $\text{SrTiO}_3$  nanocubes decorated with  $\text{Ag}/\text{AgCl}$  nanoparticles as photocatalysts with enhanced visible-light photocatalytic activity towards the degradation of dyes, phenol and bisphenol A, *Environ. Sci. Nano* 4 (2017) 585–595.
  - [45] S.J. Li, B. Xue, J.L. Chen, Y.P. Liu, J.L. Zhang, H.W. Wang, J.S. Liu, Constructing a plasmonic p-n heterojunction photocatalyst of  $3\text{D Ag}/\text{Ag}_6\text{Si}_2\text{O}_7/\text{Bi}_2\text{MoO}_6$  for efficiently removing broad-spectrum antibiotics, *Sep. Purif. Technol.* 254 (2021), 117579.
  - [46] H.Z. Deng, X.G. Fei, Y. Yang, J.J. Fan, J.G. Yu, B. Cheng, L.Y. Zhang, S-scheme heterojunction based on p-type  $\text{ZnMn}_2\text{O}_4$  and n-type  $\text{ZnO}$  with improved photocatalytic  $\text{CO}_2$  reduction activity, *Chem. Eng. J.* 409 (2021), 127377.
  - [47] Q.Z. Gao, J. Xu, Z.P. Wang, Y.F. Zhu, Enhanced visible photocatalytic oxidation activity of perylene diimide/ $\text{g-C}_3\text{N}_4$  n-n heterojunction via  $\pi$ - $\pi$  interaction and interfacial charge separation, *Appl. Catal. B Environ.* 271 (2020), 118933.
  - [48] G.D. Fan, R.S. Ning, Z.S. Yan, J. Luo, B.H. Du, J.J. Zhan, L.S. Liu, J. Zhang, Double photoelectron-transfer mechanism in  $\text{Ag}/\text{AgCl}/\text{WO}_3/\text{g-C}_3\text{N}_4$  photocatalyst with enhanced visible-light photocatalytic activity for trimethoprim degradation, *J. Hazard. Mater.* 403 (2021), 123964.
  - [49] Y.J. Shi, Y.W. Zhou, Y. Lou, Z.P. Chen, H.F. Xiong, Y.F. Zhu, Homogeneity of supported single-atom active sites boosting the selective catalytic transformations, *Adv. Sci.* (2022), 2201520.
  - [50] X.Y. Wang, J.Q. Meng, X. Yang, A. Hu, Y.X. Yang, Y.H. Guo, Fabrication of a perylene tetracarboxylic diimide-graphitic carbon nitride heterojunction photocatalyst for efficient degradation of aqueous organic pollutants, *ACS Appl. Mater. Interfaces* 11 (2019) 588–602.
  - [51] W.Y. Huang, C.W. Jing, X.D. Zhang, M.Q. Tang, L. Tang, M.H. Wu, N. Liu, Integration of plasmonic effect into spindle-shaped MIL-88A(Fe): Steering charge flow for enhanced visible-light photocatalytic degradation of ibuprofen, *Chem. Eng. J.* 349 (2018) 603–612.
  - [52] X.J. Wen, C.G. Niu, L. Zhang, D.W. Huang, G.M. Zeng, In-situ synthesis of visible-light-driven plasmonic  $\text{Ag}/\text{AgCl}/\text{CdWO}_4$  photocatalyst, *Ceram. Int.* 43 (2017) 1922–1929.
  - [53] Z. Zhu, H. Huang, L. Liu, F. Chen, N. Tian, Y. Zhang, H. Yu, Chemically bonded  $\alpha\text{-Fe}_2\text{O}_3/\text{Bi}_4\text{MO}_8\text{Cl}$  dot-on-plate Z-scheme junction with strong internal electric field for selective photo-oxidation of aromatic alcohols, *Angew. Chem. -Int. Ed.* 61 (2022), e202203519.
  - [54] L.J. Wu, S. Zheng, H. Lin, S. Zhou, A.M. Idris, J. Wang, S. Li, Z.Q. Li, In-situ assembling  $0\text{D}/2\text{D}$  Z-scheme heterojunction of lead-free  $\text{Cs}_2\text{AgBiBr}_6/\text{Bi}_2\text{WO}_6$  for

- enhanced photocatalytic CO<sub>2</sub> reduction, *J. Colloid Interface Sci.* 629 (2023) 233–242.
- [55] D. Wang, Y. Li, Y. Jiang, X. Cai, X. Yao, Perspectives on surface chemistry of nanostructured catalysts for heterogeneous advanced oxidation processes, *Environ. Funct. Mater.* 1 (2022) 182–186.
- [56] P. Raizada, P. Thakur, A. Sudhaik, P. Singh, V.K. Thakur, A. Hosseini-Bandegharai, Fabrication of dual Z-scheme photocatalyst via coupling of BiOBr/Ag/AgCl heterojunction with P and S co-doped g-C<sub>3</sub>N<sub>4</sub> for efficient phenol degradation, *Arab. J. Chem.* 13 (2020) 4538–4552.
- [57] R. Acosta-Herazo, M.A. Mueses, G. Li Puma, F. Machuca-Martinez, Impact of photocatalyst optical properties on the efficiency of solar photocatalytic reactors rationalized by the concepts of initial rate of photon absorption (IRPA) dimensionless boundary layer of photon absorption and apparent optical thickness, *Chem. Eng. J.* 356 (2019) 839–849.
- [58] D. Dolat, N. Quici, E. Kusiak-Nejman, A.W. Morawski, G.L. Puma, One-step, hydrothermal synthesis of nitrogen, carbon co-doped titanium dioxide (N,C-TiO<sub>2</sub>) photocatalysts. Effect of alcohol degree and chain length as carbon dopant precursors on photocatalytic activity and catalyst deactivation, *Appl. Catal. B Environ.* 115 (2012) 81–89.
- [59] D. Wang, M. Angel Mueses, J.A. Colina Marquez, F. Machuca-Martinez, I. Grcic, R. P. Muniz Moreira, G. Li Puma, Engineering and modeling perspectives on photocatalytic reactors for water treatment, *Water Res.* 202 (2021), 117421.
- [60] I. Grcic, G.L. Puma, Six-flux absorption-scattering models for photocatalysis under wide-spectrum irradiation sources in annular and flat reactors using catalysts with different optical properties, *Appl. Catal. B Environ.* 211 (2017) 222–234.
- [61] S. Suzuki, M. Ogo, T.W. Miller, A. Shimizu, H. Takada, M.A.T. Siringan, Who possesses drug resistance genes in the aquatic environment?: Sulfamethoxazole (SMX) resistance genes among the bacterial community in water environment of Metro-Manila, Philippines, *Front. Microbiol.* 4 (2013) 102.
- [62] L.S. Cai, J.Y. Sun, F. Yao, Y.M. Yuan, M. Zeng, Q.X. Zhang, Q.D. Xie, S.W. Wang, Z. Wang, X.Y. Jiao, Antimicrobial resistance bacteria and genes detected in hospital sewage provide valuable information in predicting clinical antimicrobial resistance, *Sci. Total Environ.* 795 (2021), 148815.
- [63] W.X. Zhao, B. Wang, G. Yu, Antibiotic resistance genes in China: Occurrence, risk, and correlation among different parameters, *Environ. Sci. Pollut. Res.* 25 (2018) 21467–21482.
- [64] L.F. Ning, J. Xu, Y. Lou, C.S. Pan, Z.P. Wang, Y.F. Zhu, A 3D/0D cobalt-embedded nitrogen-doped porous carbon/supramolecular porphyrin magnetic-separation photocatalyst with highly efficient pollutant degradation and water oxidation performance, *J. Mater. Sci. Technol.* 124 (2022) 53–64.
- [65] Y.F. Wang, M. Zhang, J. Li, H.C. Yang, J. Gao, G. He, Z.Q. Sun, Construction of Ag@AgCl decorated TiO<sub>2</sub> nanorod array film with optimized photoelectrochemical and photocatalytic performance, *Appl. Surf. Sci.* 476 (2019) 84–93.
- [66] M.K. Kumar, G. Naresh, V.V. Kumar, B.S. Vasista, B. Sasikumar, A. Venugopal, Improved H<sub>2</sub> yields over Cu-Ni-TiO<sub>2</sub> under solar light irradiation: Behaviour of alloy nano particles on photocatalytic H<sub>2</sub>O splitting, *Appl. Catal. B Environ.* 299 (2021), 120654.
- [67] X. Chen, J. Wang, Y. Chai, Z. Zhang, Y. Zhu, Efficient photocatalytic overall water splitting induced by the giant internal electric field of a g-C<sub>3</sub>N<sub>4</sub>/rGO/PDIP Z-scheme heterojunction, *Adv. Mater.* 33 (2021), 2007479.
- [68] K.E. Brown, W.A. Salamant, L.E. Shorer, R.M. Young, M.R. Wasielewski, Direct observation of ultrafast excimer formation in covalent perylenediimide dimers using near-infrared transient absorption spectroscopy, *J. Phys. Chem. Lett.* 5 (2014) 2588–2593.
- [69] Z. Zhong, R. Li, W. Lin, X. Xu, X. Tian, X. Li, X. Chen, L. Kang, One-dimensional nanocrystals of cobalt perylene diimide polymer with in-situ generated FeOOH for efficient photocatalytic water oxidation, *Appl. Catal. B Environ.* 260 (2020), 118135.
- [70] Y.N. Zhang, D. Wang, W.X. Liu, Y. Lou, Y. Zhang, Y.M. Dong, J. Xu, C.S. Pan, Y. F. Zhu, Create a strong internal electric-field on PDI photocatalysts for boosting phenols degradation via preferentially exposing  $\pi$ -conjugated planes up to 100%, *Appl. Catal. B Environ.* 300 (2022), 120762.
- [71] Y. Sheng, W. Li, L. Xu, Y. Zhu, High photocatalytic oxygen evolution via strong built-in electric field induced by high crystallinity of perylene imide supramolecule, *Adv. Mater.* 34 (2022), 2102354.
- [72] D.S. Lei, J.Q. Xue, X.Y. Peng, S.H. Li, Q. Bi, C.B. Tang, L. Zhang, J. Zhang, Effective photocatalytic removal of As(III) by ZnFe<sub>2</sub>O<sub>4</sub>/Ag/AgCl coupled peroxymonosulfate: Z-scheme charge transfer and dual active sites, *Appl. Surf. Sci.* 567 (2021), 150860.
- [73] G. Zhang, T. Dai, Y. Meng, L. Zhang, C. Yang, G. Pan, Z. Ni, S. Xia, Z-Scheme heterojunction ZnO-Au-ZnAl<sub>2</sub>O<sub>4</sub>: bridge-type hot carrier transfer and reaction kinetics in the photodegradation of catechol, *Appl. Surf. Sci.* 532 (2020), 147456.
- [74] Y. Huo, J.F. Zhang, K. Dai, Q. Li, J.L. Lv, G.P. Zhu, C.H. Liang, All-solid-state artificial Z-scheme porous g-C<sub>3</sub>N<sub>4</sub>/Sn<sub>2</sub>S<sub>3</sub>-DETA heterostructure photocatalyst with enhanced performance in photocatalytic CO<sub>2</sub> reduction, *Appl. Catal. B Environ.* 241 (2019) 528–538.
- [75] F. Guo, H. Zhang, H. Li, Z.R. Shen, Modulating the oxidative active species by regulating the valence of palladium cocatalyst in photocatalytic degradation of ciprofloxacin, *Appl. Catal. B Environ.* 306 (2022), 121092.
- [76] J. Xu, Q.Z. Gao, Z.P. Wang, Y. Zhu, An all-organic 0D/2D supramolecular porphyrin/g-C<sub>3</sub>N<sub>4</sub> heterojunction assembled via  $\pi$ - $\pi$  interaction for efficient visible photocatalytic oxidation, *Appl. Catal. B Environ.* 291 (2021), 120059.
- [77] F. Wang, J. Xu, Z.P. Wang, Y. Lou, C.S. Pan, Y.F. Zhu, Unprecedentedly efficient mineralization performance of photocatalysis-self-Fenton system towards organic pollutants over oxygen-doped porous g-C<sub>3</sub>N<sub>4</sub> nanosheets, *Appl. Catal. B Environ.* 312 (2022), 121438.
- [78] J. Xu, Q.Z. Gao, X.J. Bai, Z.P. Wang, Y.F. Zhu, Enhanced visible-light-induced photocatalytic degradation and disinfection activities of oxidized porous g-C<sub>3</sub>N<sub>4</sub> by loading Ag nanoparticles, *Catal. Today* 332 (2019) 227–235.
- [79] G.D. Fan, X.M. Zheng, J. Luo, H.P. Peng, H. Lin, M.C. Bao, L. Hong, J.J. Zhou, Rapid synthesis of Ag/AgCl@ZIF-8 as a highly efficient photocatalyst for degradation of acetaminophen under visible light, *Chem. Eng. J.* 351 (2018) 782–790.
- [80] G.D. Fan, Z. Chen, Z.S. Yan, B.H. Du, H.L. Pang, D.S. Tang, J. Luo, J.Y. Lin, Efficient integration of plasmonic Ag/AgCl with perovskite-type LaFeO<sub>3</sub>: enhanced visible-light photocatalytic activity for removal of harmful algae, *J. Hazard. Mater.* 409 (2021), 124062.